A hetero-epitaxially grown zeolite film and its unprecedented use as a perm-selective membrane

Yanghwan Jeong,[1] Sungwon Hong,[1] Eunhee Jang,[1] Eunjoo Kim,[1]

Hionsuck Baik,[2] Nakwon Choi,[3] Alex C.K. Yip,[4] and Jungkyu Choi[1,*]

[1] Department of Chemical & Biological Engineering, College of Engineering, Korea University, 145 Anam-ro, Seongbuk-gu, Seoul 02841, Republic of Korea

[2] Korea Basic Science Institute (KBSI), Seoul Center, 145 Anam-ro, Seongbuk-gu, Seoul 02841, Republic of Korea

[3] Center for BioMicrosystems, Brain Science Institute, Korea Institute of Science and Technology (KIST), Hwarang-ro 14-gil, Seongbuk-gu, Seoul 02792, Republic of Korea

[4] Chemical and Process Engineering, University of Canterbury, Private Bag 4800, Christchurch, New Zealand

* Corresponding Author

E-mail address: jungkyu_choi@korea.ac.kr, Phone: +82-2-3290-4854, and Fax: +82-2-926-6102

Abstract

The secondary growth methodology to form zeolite membranes involves covering the surface of a porous support with zeolite seed particles and using a hydrothermal process to close gaps between the seeds. However, stringent requirements for homogeneous epitaxial inter-growth of the seed layer limit the number of high-quality zeolite membranes. Here, to the best of our knowledge, we, for the first time, report the successful hetero-epitaxial growth of highly siliceous ZSM-58 (DDR type zeolite) films from a SSZ-13 (CHA type zeolite) seed layer. This originated from the structural compatibility of the CHA and DDR zeolites. The resulting films, now membranes, showed excellent CO_2 perm-selectivities. Furthermore, the hybrid membrane mainly comprised all-silica DDR constituents and, thus, well preserved the CO_2 perm-selectivity in the presence of H_2O vapor.

One Sentence Summary: A hetero-epitaxial growth of a SSZ-13 zeolite seed layer with the ZSM-58 precursor allowed for forming a CO_2 perm-selective hybrid membrane.

Membrane technology has applications in the fields of refining, petrochemicals, and natural gas industries. Advantageous features of membrane technology for gas separation include the high energy efficiency, simple/compact process operation, and low environmental pollution compared to conventional methods that rely on distillation, sorption, and re-crystallization (*1-3*)***Error! Bookmark not defined.***. With these advantages, membrane technology is also promising for CO_2 relevant separation processes (*4-6*). The threat of global warming and climate change has drawn world-wide attention to energy-efficient CO_2 capture (*7*). Thus, post combustion carbon capture has been recognized as an essential way to reduce the amount of CO_2 emissions to the atmosphere. Among the various inorganic materials, crystalline aluminosilicates, i.e., zeolites, are well known for their molecular sieving ability, allowing the differentiation of molecular transport via regular and rigid micropores (*8, 9*). Nowadays, the fabrication of supported zeolite membranes primarily uses the secondary growth methodology (*10-12*). In this process, zeolite seed particles are uniformly deposited on the support and, subsequently, the same type of zeolite is homogeneously grown from the seed particles through hydrothermal reaction, thus forming a continuous membrane. Despite the high reproducibility of this approach, the protocol relies on homogeneous epitaxial growth to form the structured zeolite films, thus limiting the number of zeolites of the 234 types that can be used to form membranes (*13-16*).

One type of zeolite, the deca-dodecasil 3 rhombohedral (DDR) type zeolite, which has an 8-membered ring (MR) motif, has a pore size of 0.36 × 0.43 nm^2. This specific pore aperture is highly desirable for the membrane-based continuous separation of CO_2 (kinetic diameter of 0.33 nm) from slightly larger molecules; e.g., CH_4 (0.38 nm) in natural/shale gas and biogas upgrading and N_2 (0.364 nm) in post-combustion carbon capture (*17, 18*). However, the conventional method to synthesize DDR zeolite particles is very complicated and time-consuming (*19*). Although alternative synthesis approaches for DDR zeolites have been proposed to reduce the reaction time and simplify the synthetic conditions (*20-24*), other zeolite phases such as sigma-2 (SGT) or dodecasil 1 hexagonal (DOH) are often uncontrollably co-synthesized arising from the use of the same structure directing agent (1-adamantylamine) (*25, 26*). In addition, the

particle size of DDR zeolites has a wide distribution so that it is quite difficult to produce a uniform seed layer, which is critical for the formation of a continuous membrane via epitaxial growth (*23*). Thus, the formation of continuous membranes based on the secondary growth methodology is inhibited.

In this study, SSZ-13 (CHA; chabazite) particles were used as seeds and the corresponding seed layer was further inter-grown with a synthetic precursor that allows for the formation of DDR zeolites. This heterogeneous synthetic approach was attempted here because of the structural compatibility between the CHA and DDR type zeolites. We verified the structural compatibility-based growth in the resulting hetero-epitaxially grown DDR@CHA (representing DDR zeolite growth from CHA seed layer; analogous to shell@core zeolite structure synthesis (*27*)) films or membranes through transmission electron microscopy analysis. Furthermore, we investigated the CO_2 perm-selectivity ability of the membrane. Although heterogeneously structured zeolite films or layers have been reported before (*28-32*), to the best of our knowledge, our heterogeneous but well inter-grown DDR@CHA membrane, for the first time, showed remarkable CO_2-selective separation performance with respect to industrially relevant feeds. In addition, although some composite zeolite membranes were fabricated previously, their formation did not originate purely from heteroepitaxial growth between two different types of zeolites (*33, 34*). Finally, we have tested the CO_2 separation performance of the DDR@CHA membrane and its robustness under humid conditions because water vapor is the third largest component in both flue gas and natural/biogas streams.

Properties of heterogeneously grown zeolite membranes

Fig. 1A shows a SEM image of the particles, which were synthesized with a nominal Si/Al ratio of ~20. The average size of these particles was 230 ± 70 nm (fig. S1), which is highly suitable for use as seed particles on top of a porous support. The XRD patterns in Fig. 1C confirm that the synthesized particles were composed of the CHA zeolite phase known as standard oil synthetic zeolite-13 (SSZ-13). Fig. 1B shows that the SSZ-13 particles were closely packed and well-dispersed over the surface of the porous α-Al_2O_3 disc, thus forming a uniform SSZ-13 seed layer. Its corresponding XRD pattern in Fig. 1C supports

the formation of the uniform layer with SSZ-13 particles of high crystalline purity on the α-Al_2O_3 disc. For convenience, the hetero-epitaxially grown membrane is referred to as SZ_*x*d, where S stands for a SSZ-13 seed layer, Z represents the ZSM-58 portion after secondary growth, and *x* indicates the hydrothermal secondary growth time in days. Fig. 1, D and E reveal that the 6-d hydrothermal growth (i.e., SZ_6d) of the seed layer shown in Fig. 1B with the synthetic precursor that allowed for the synthesis of ZSM-58 (DDR type zeolite) resulted in effective covering of the SSZ-13 layer, apparently because of its compatible growth with the DDR type zeolite. The co-existence of the SSZ-13 seed layer at the bottom and the DDR-structured portion at the top in a several-micrometer thick film (~4.3 μm), as shown in Fig. 1E, is supported by the XRD pattern in Fig. 1F. It appears that a heterogeneous zeolite film was formed after the secondary growth of a SSZ-13 (CHA type zeolite) layer with the ZSM-58 (DDR type zeolite) synthetic precursor. Furthermore, Fig. 1, G and H show that after increasing the hydrothermal growth time to 10 d, the DDR-structured portion of SZ_10d became pronounced, as reflected by the formation of a continuous film with an increased total thickness of ~7 μm (Fig. 1H). Because the major portion is the DDR constituent or grain, the XRD peaks corresponding to the SSZ-13 layer in SZ_10d became negligible (Fig. 1I), indicating that the SSZ-13 layer was well embedded and non-detectable.

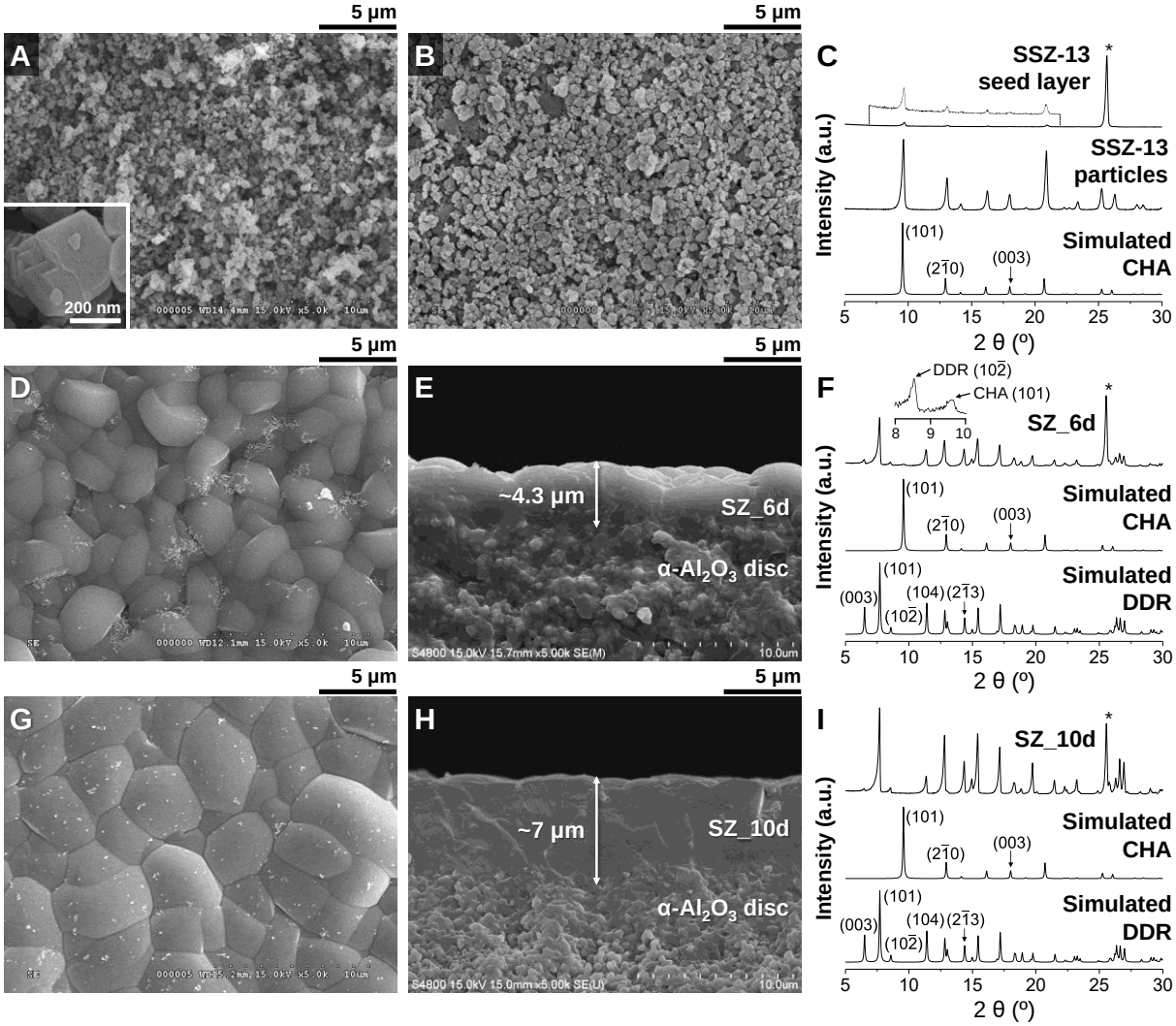

Fig. 1. Seed layer and its hetero-epitaxial growth toward a continuous film. SEM images of (**A**) SSZ-13 seed particles and (**B**) a SSZ-13 seed-coated α-Al_2O_3 disc, and (**C**) XRD patterns of the seed particles and the seed layer shown in (A and B). (**D** and **G**) Top view and (**E** and **H**) cross-sectional view SEM images of (D and E) SZ_6d and (G and H) SZ_10d grown from SSZ-13 seed layers, and (**F** and **I**) XRD patterns of (F) SZ_6d and (I) SZ_10d. In (C and F), for a clear view, the magnified XRD patterns of the SSZ-13 seed layer and SZ_6d are shown above their normalized XRD patterns. In addition, the simulated XRD patterns of all-silica DDR and CHA zeolites are added at the bottom of the graphs. Finally, the asterisks (*) denote the XRD peaks from the α-Al_2O_3 disc.

First, we investigated how well the ZSM-58 zeolite was structurally incorporated with the SSZ-13 seed layer to form a continuous hybrid film. In particular, we focused on investigating the compatibility between the ZSM-58 grain and the SSZ-13 seed layer through the TEM-based visualization of their interface and its surrounding area. The cross-sectioned SZ_6d, whose higher magnification SEM image is also shown in Fig. 2A, was used to obtain the TEM image shown in Fig. 2B and STEM images in Fig. 2, C and D. Spots with different contrast (220 ± 60 nm, estimated from measuring 21 dark spots in Fig. 2C), indicated by orange arrows in the bottom of the membrane in Fig. 2, B and C, were easily observed throughout the cross-sectional images. Their position close to the α-Al_2O_3 disc suggests that these spots were related to the 230-nm-sized SSZ-13 seed particles. In addition, the irregular, but globular shape of these different contrast spots supports their identification as seed particles, as shown in Fig. 1, A and B. Subsequently, in an effort to distinguish the CHA and DDR zeolite domains in SZ_6d, we acquired the diffraction patterns in the area marked "E" in Fig. 2D inside one dark spot (seemingly related to SSZ-13 seed particles) and "F" in Fig. 2D between dark spots (seemingly related to heterogeneously grown DDR grains). The resulting diffraction patterns are shown in Fig. 2, E and F along with the corresponding simulated patterns (red dots). We found that the diffraction pattern in Fig. 2E was well matched by the simulated diffraction pattern according to the CHA zeolite-based $[4\,1\,\overline{14}]$ zone axis. Likewise, the diffraction pattern in Fig. 2F was well described by the simulated diffraction pattern corresponding to the [871] zone axis of the DDR zeolite. For better demonstration, the simulated diffraction patterns with respect to the $[4\,1\,\overline{14}]$ zone axis of the CHA zeolite and the [871] zone axis of the DDR zeolite are displayed next to the experimental diffraction patterns in fig. S2. These TEM-based analyses suggest that SZ membrane comprised two heterogeneous phases (DDR as a major portion and CHA as a seed layer) and, thus, had been formed by the inter-growth of SSZ-13 particles with the DDR phase in-between. In addition, SZ_4d, which was not significantly inter-grown because of the shorter growth time (refer to the cross-sectional SEM image in fig. S3A), contained the aforementioned dark spots in its STEM image (fig. S3B). Structural analysis of the electron diffraction pattern also supported the co-existence of the CHA and DDR zeolite phases inside SZ_4d (fig. S3, C and D).

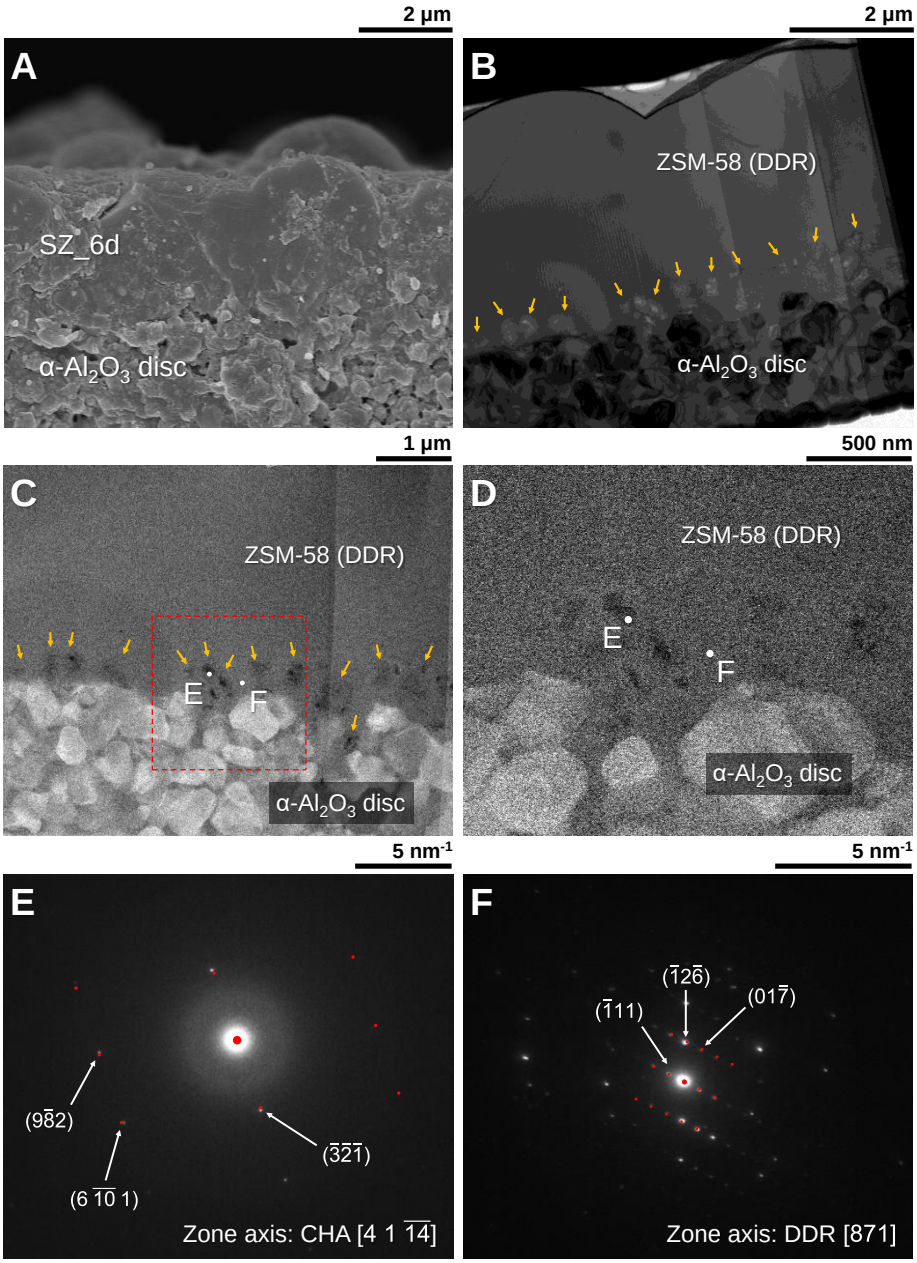

Fig. 2. Identification of the CHA and DDR zeolite phases in the hetero-epitaxially grown zeolite film. Cross-sectional view (**A**) SEM, (**B**) TEM, and (**C** and **D**) STEM images of SZ_6d. In (B and C), the orange arrows indicate the SSZ-13 seed particles. (**E** and **F**) Electron diffraction patterns obtained from the white dots labeled "E" and "F" in (C and D); the corresponding simulated patterns (*red dots*) are superimposed on the experimental patterns. The simulated diffraction patterns in (E and F) are obtained along the [4 1 $\bar{1}$4] zone axis in the CHA zeolite and the [871] zone axis in the DDR zeolite, respectively. In addition, the Miller indices are included on each electron diffraction pattern.

Based on this presumed hetero-epitaxial growth, in fig. S4, we propose a plausible structure model that can account for the hetero-epitaxial growth at the interface between the CHA and DDR type zeolites. Specifically, both CHA and DDR zeolites have a trigonal crystal system of the hexagonal crystal family and the corresponding space group is *R*3*m* ($a = b \neq c$ along with $\alpha = 90°$, $\beta = 90°$, and $\gamma = 120°$). In addition, note that the dimensions of the *a*- and *b*-axes of the unit cells are very similar (CHA zeolite, *a*: 13.6750 Å, *b*: 13.6750 Å, and *c*: 14.7670 Å and DDR zeolite, *a*: 13.7950 Å, *b*: 13.7950 Å, and *c*: 40.7500 Å). It appears that this structural compatibility of the CHA and DDR zeolites, especially for the inter-growth along the *c*-axis, was key to achieving hetero-epitaxial growth from the SSZ-13 seed layer toward the DDR zeolite phase and forming a continuous hybrid film. As expected, the other synthetic direction (i.e., hetero-epitaxial growth of a DDR seed layer toward the major CHA phase) worked well (fig. S5). However, the hydrothermal growth of the SSZ-13 seed layer with a MFI zeolite synthetic precursor did not lead to continuous film formation (fig. S6), as they did not share structural similarities.

The membrane properties of the SZ membrane series (SZ_*x*d; *x* = 4, 6, 8, 10, and 12) were investigated (table S1 and figs. S7 to S10). As the secondary growth time increased, the film surface became gradually dense with an increased grain size. In addition, all the membrane properties of thickness, hydrophobicity, and out-of-plane orientation were monotonically increased with secondary growth time. Detailed results and discussion regarding the various approaches in hetero-epitaxial growths and the membrane properties of the SZ membrane series are given in the supplementary materials.

CO_2 perm-selectivities of SZ membranes

In fig. S11, A to E, the permeances of CO_2 and N_2 molecules and the corresponding CO_2/N_2 SFs of SZ_*x*d (*x* = 4, 6, 8, 10, and 12) with respect to the dry equimolar CO_2/N_2 feed mixture are plotted as a function of temperature. For a better comparison, the separation performances of the SZ membrane series measured at 30 °C, where the maximum (max) CO_2/N_2 SF was observed, are illustrated in fig. S11F. SZ_4d showed the lowest separation performance with the max CO_2/N_2 SF being as low as ~1.1, indicating that it

was not sufficiently inter-grown. However, additional growth resulted in the monotonic increase in the CO_2/N_2 SF, reaching asymptotic behavior after ~10 d; apparently, the film growth was almost saturated after ~10 d (in good agreement with the thickness trend listed in table S1).

Fig. 3, A to D shows the separation performances of SZ_10d as a function of temperature with respect to both equimolar CO_2/N_2 and CO_2/CH_4 binary mixtures. In particular, we considered dry (Fig. 3, A and C) and wet (Fig. 3, B and D) feeds to observe the effect of water vapor, the 3rd largest component in the flue gas of fossil fuel-fired power plants (relevant to CO_2/N_2 separation) and biogas (relevant to CO_2/CH_4 separation), on the separation performance. First, under dry conditions, the CO_2 permeances monotonically decreased with temperature, whereas the permeance of the other permeating component (N_2 or CH_4) did not vary with temperature. This CO_2 permeance behavior with temperature was very similar for both the CO_2/N_2 and CO_2/CH_4 mixtures, indicating the pronounced contribution of the preferred adsorption of CO_2 (*35*). This separation trend is comparable to that of the homogeneous ZSM-58 membrane reported in our previous study (*14*), indicating the major portion of DDR zeolites in the DDR@CHA hybrid film. The highest SFs were observed at the lowest temperature of 30 °C considered in this study for both CO_2/N_2 and CO_2/CH_4 separations, specifically, max CO_2/N_2 SF of 15.2 ± 0.4 and max CO_2/CH_4 SF of 279 ± 38. It was noted that despite the extremely slight size difference between N_2 (0.364 nm) and CH_4 (0.38 nm), the corresponding SFs were dramatically different, indicating the high sensitivity of the molecular sieving ability to the size of the guest molecules.

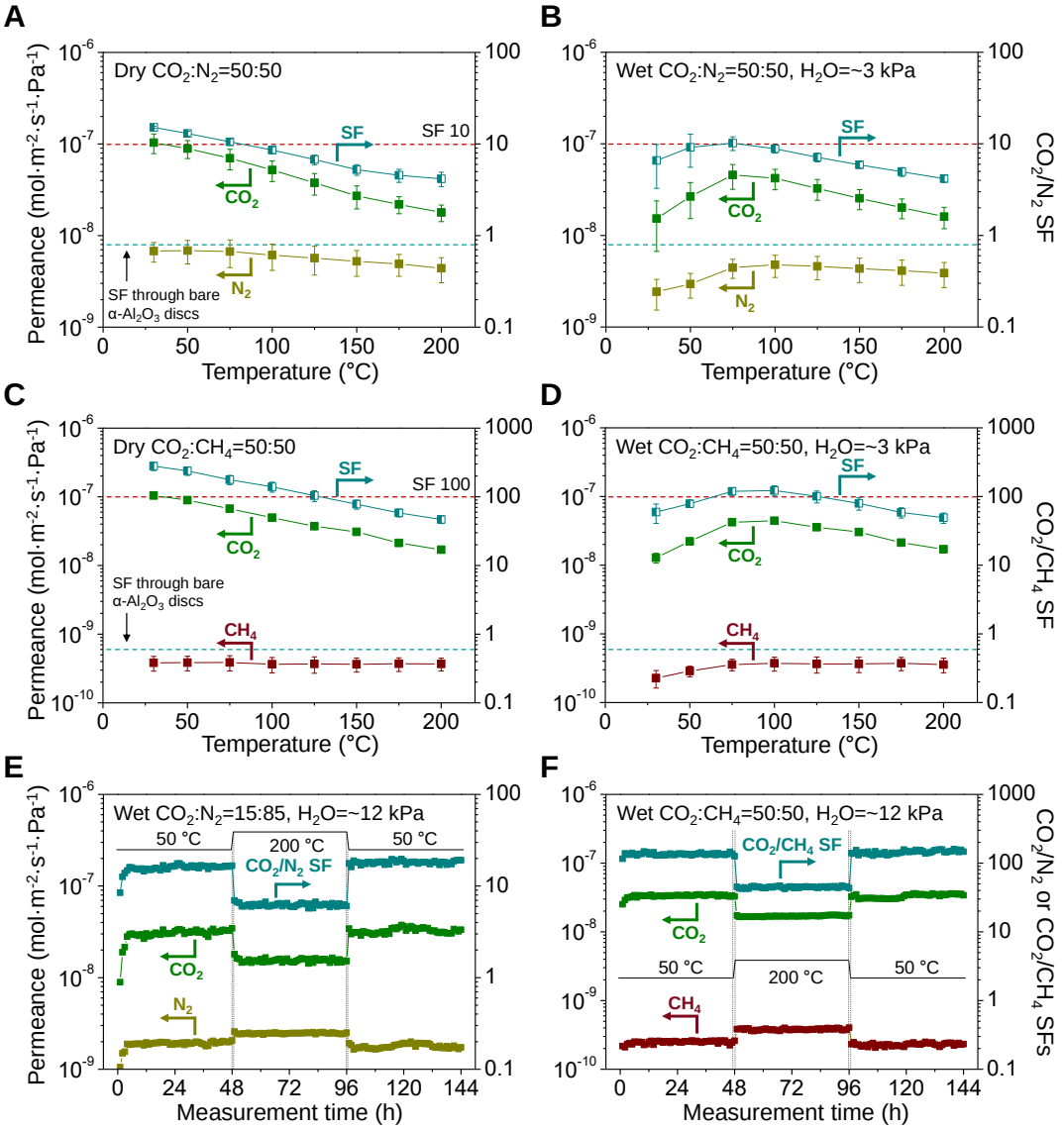

Fig. 3. CO_2 perm-selectivities and stability tests of the hetero-epitaxially grown SZ membrane. Permeances and SFs of SZ_10d with respect to equimolar (**A** and **B**) CO_2/N_2 and (**C** and **D**) CO_2/CH_4 binary feed mixtures under dry and wet conditions. The red dashed lines indicate a CO_2/N_2 SF of 10 in (A and B) and a CO_2/CH_4 SF of 100 in (C and D). The cyan dashed lines indicate a CO_2/N_2 SF of 0.8 in (A and B) and a CO_2/CH_4 SF of 0.6 in (C and D), which were determined assuming Knudsen diffusion and observed for a bare α-Al_2O_3 disc. In addition, the stability tests of SZ_10d were conducted at 50 °C for up to 4 d with H_2O vapor (~12 kPa) with respect to (**E**) CO_2/N_2 binary feed mixtures composed of 15% CO_2 and 85% N_2 and (**F**) equimolar CO_2/CH_4 binary feed mixtures; harsh conditions at 200 °C for 2 d were used to simulate long-term use.

Compared to dry conditions, we observed unique permeation behavior of CO_2 and the slowly permeating component (N_2 or CH_4) in the wet feed (Fig. 3, B and D). In particular, at a low temperature of ~30-100 °C, the permeances of all the permeating components (CO_2, N_2, and CH_4) were reduced possibly because of the inhibition of adsorbed water molecules on the membrane surface under wet conditions (*36*). As the adsorption of water vapor weakened with increasing temperature, the permeances of CO_2 and the other components, as well as the corresponding SFs, were gradually increased from 30 to 75 °C; this is equivalent to the recovery to the values observed under dry conditions (Fig. 3, A and C). Indeed, above 100 °C, the permeances and SFs were fully recovered to those obtained under dry conditions. Interestingly, the degree of reduction of CO_2 permeance because of water vapor was higher than those of the other very slowly permeating components (Fig. 3, A to D), resulting in a decrease in the corresponding SF at ~30-75 °C under wet conditions. Nevertheless, the CO_2 perm-selectivities of SZ_10d were quite high, even in the presence of water vapor: CO_2/N_2 SF of 9.1 ± 3.6 and CO_2/CH_4 SF of 78 ± 9 at 50 °C. Considering that the flue gas from coal-fired power plants and biogas streams contain water vapor of up to ~12 kPa and the temperature ranges from ~50 to 60 °C (*37-40*), hydrophobic SZ_10d is highly expected to show reliable CO_2 perm-selectivities for these applications. In addition, the separation performance of SZ_10d under more realistic post-combustion feed conditions was almost identical to those shown in Fig. 3, A and B; SZ_10d showed an almost linear response to the change in CO_2 partial pressures in the feed, apparently due to the linear adsorption behavior of CO_2 molecules (figs. S12 to S13). This supports the reliable and flexible availability of SZ_10d with respect to various or fluctuating molar compositions of CO_2 molecules. Detailed information is given in the supplementary materials.

One primary benefit in the use of zeolite membranes is their robustness, which makes them suitable for long-term practical applications. To test the robustness, SZ_10d was exposed to wet equimolar CO_2/N_2 feeds at 50 and 75 °C, which are representative flue gas temperatures (fig. S14A). At each temperature, there was no apparent deactivation or declining trend in the performance for up to 3 d, indicating the robustness of SZ_10d. In addition, we investigated the effect of the relative humidity on the

performances of SZ_10d (fig. S14B). Specifically, after 6-h measurement at 50 °C under dry conditions (i.e., 0% relative humidity) with a CO_2:N_2 = 15:85 simulated flue gas composition, we measured the performances as a function of relative humidity (~26%, ~60%, and ~100%) at 50 °C for 12 h in each case (fig. S14B). At each relative humidity, the CO_2 permeances and CO_2/N_2 SFs through SZ_10d were well maintained, supporting the desirable properties of the hydrophobic zeolite membranes. Furthermore, we tested the CO_2 perm-selectivities of SZ_10d with respect to a realistic wet flue gas from a coal-fired power plant with a water vapor pressure of ~12 kPa (100% relative humidity) at 50 °C (Fig. 3E). Initial tests for up to 2 d show a reliable CO_2 perm-selectivity with the corresponding CO_2/N_2 SF being ~17. In addition, we attempted to accelerate deactivation, if any, by increasing the temperature to 200 °C for 2 d. Nevertheless, the CO_2 perm-selectivity of SZ_10d was well preserved for up to an additional 2 d (Fig. 3E), strongly supporting the high long-term stability. In the same manner, we tested the CO_2 perm-selectivity of SZ_10d at 50 °C with respect to a wet equimolar CO_2/CH_4 mixture at a water vapor pressure of ~12 kPa (Fig. 3F). This long-term stability test clearly demonstrates the robustness of SZ_10d, which is required for reliable use in real separation processes.

Defect structures in the SZ membrane series

Fig. 4 shows both the cross-sectional and top view SEM and FCOM images of SZ_6d and SZ_10d. In particular, these two membranes were chosen for FCOM analysis because SZ_6d and SZ_10d showed marked difference in their CO_2 perm-selectivities under dry conditions (fig. S11, B and D). The dye molecules (fluorescein sodium salt) with an estimated size of ~1 nm (*41, 42*) cannot penetrate into the zeolitic pores (smaller than ~1 nm) but can fully access into the defects in the zeolite membrane (*14, 42, 43*). Clearly, both SZ_6d and SZ_10d contained cracks propagating down to the interface between the SZ membrane and the α-Al_2O_3 disc. The appearance of such cracks was pronounced in terms of density and frequency for SZ_6d, indicating that it is more defective than SZ_10d. This trend is quite clear in their top view FCOM images in Fig. 4, F and H. In fact, the defect density can be directly associated with the CO_2-

selective separation performance shown in Fig. 3 and fig. S11; SZ_10d contained fewer defects than SZ_6d and, thus, provided much higher CO_2/N_2 SFs under dry conditions (~15.2 for SZ_10d vs. ~6.0 for SZ_6d). For comparison, the FCOM results of other membranes (SZ_8d and SZ_12d) are displayed along with those of SZ_6d and SZ_10d in figs. S15 to S16. It appears that as the secondary growth time was increased from 6 to 12 d, the membrane thicknesses monotonically increased and became saturated after 10 d, but the degree of defects showed the opposite, monotonically decreasing trend up to 10 d, subsequently becoming steady. This indicates that the greater thickness arising from the additional inter-growth of DDR grains in the DDR@CHA hybrid structure was desirable in avoiding crack formation after the calcination processes.

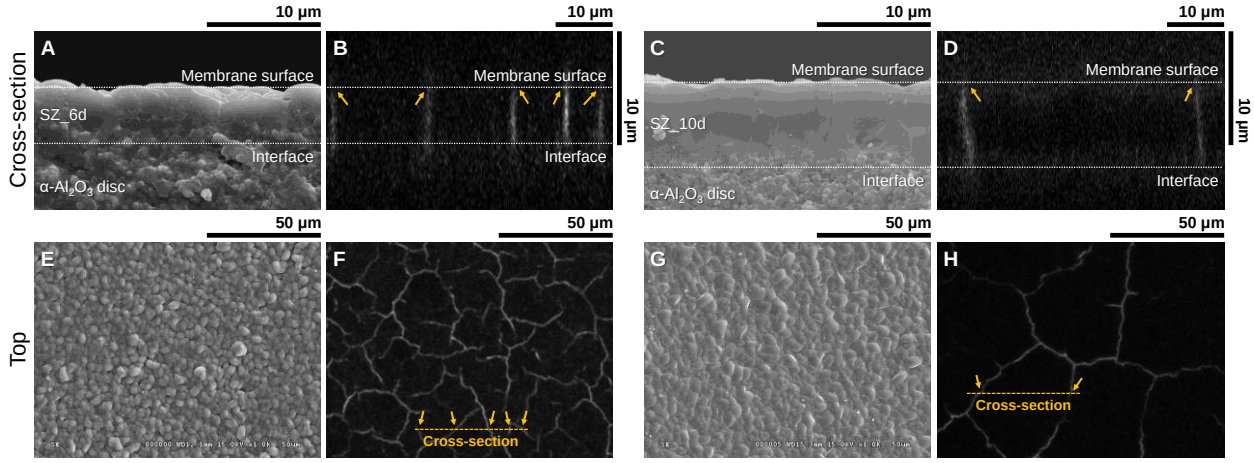

Fig. 4. Visualization of defects inside the hetero-epitaxially grown SZ membrane series. Cross-sectional view (**A** and **C**) SEM and (**B** and **D**) FCOM images of (A and B) SZ_6d and (C and D) SZ_10d. In (B and D), the upper and lower white dashed lines indicate the membrane surface and the interface between membrane and α-Al_2O_3 disc. Top view (**E** and **G**) SEM images and (**F** and **H**) FCOM images of (E and F) SZ_6d and (G and H) SZ_10d, respectively. The cross-sectional view FCOM images were obtained at the orange dashed lines in the top view FCOM images. For clarification, orange arrows are included to point to the defects present in each membrane. The top view FCOM images of SZ_6d and SZ_10d were obtained at approximately 2 and 3.5 µm below the membrane surface, respectively

Evaluation of the separation performance of SZ_10d

The CO_2/N_2 and CO_2/CH_4 separation performances of SZ_10d investigated at ~50-60 °C are displayed along with those of other zeolite membranes reported in the literature (Fig. 5, A and B). In particular, the performances of zeolite membranes tested under both dry (filled symbols) and wet (open symbols) conditions are collected and shown in Fig. 5. The hetero-epitaxially grown SZ_10d showed marked separation performance under both dry and wet conditions, and these are comparable to or superior to those of homogeneously-grown CHA type (CHA, (*42, 44*); SSZ-13, (*13*); and SAPO-34 (*45*)), DDR type (DDR (*46*) and ZSM-58 (*14*)), and FAU type (*15*) zeolite membranes. This indicates the reliability of the hybrid film formation methodology used in this study. Under dry conditions, SZ_10d showed separation performance similar or superior to those of CHA and DDR zeolite type membranes (Fig. 5A). In contrast, a very hydrophilic FAU type zeolite (NaY) membrane showed slightly higher CO_2/N_2 SFs under dry conditions but this deteriorated significantly under wet conditions, apparently because of the preferred adsorption of water vapor over CO_2 molecules. Although the use of very hydrophilic FAU zeolites as membrane constituents is a sound approach for dry feeds, these membranes are not feasible for ensuring high CO_2 perm-selectivities in wet feeds. More desirably, the hydrophobic SZ_10d, which was effectively hetero-epitaxially grown, showed high performance even in actual flue gas conditions (CO_2:N_2 = 15:85 at 50 °C with H_2O vapor pressure of ~12 kPa) (Fig. 5A).

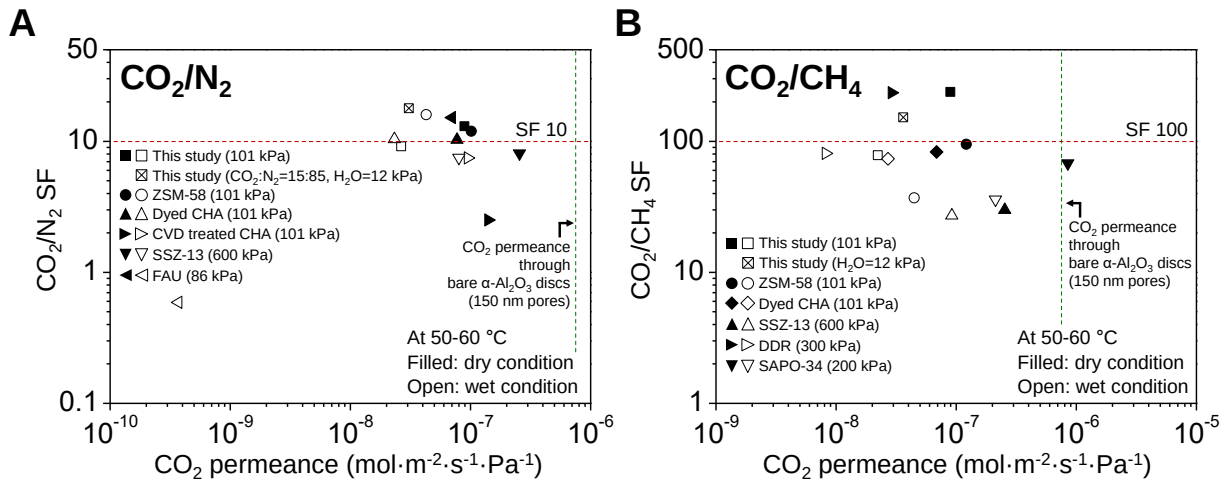

Fig. 5. Evaluation of separation performances of the hetero-epitaxially grown SZ membrane. SFs vs. CO_2 permeances of SZ_10d (this study) and other reported zeolite membranes in equimolar (**A**) CO_2/N_2, and (**B**) CO_2/CH_4 binary feed mixtures at 50-60 °C under dry (filled) and wet (open) conditions. For CO_2/N_2 separation, the performances of ZSM-58 (homogeneous DDR), (*14*); dyed, (*42*); or chemical vapor deposition (CVD)-treated CHA, (*44*); SSZ-13, (*13*); and FAU (*15*) zeolite membranes are shown. In addition, for CO_2/CH_4 separation, the performances of ZSM-58 (homogeneous DDR), (*14*); dyed CHA, (*42*); SSZ-13, (*13*); DDR, (*46*); and SAPO-34 (*45*) membranes are shown. For comparison, the total feed pressure or measurement conditions of each separation performance are displayed next to the introductory remarks about the membranes. The red dashed lines in (A and B) indicate a CO_2/N_2 SF of 10 and a CO_2/CH_4 SF of 100, respectively. The green dashed lines indicate CO_2 permeance in the equimolar CO_2/N_2 and CO_2/CH_4 binary feed mixtures through Knudsen diffusion of a bare α-Al_2O_3 disc with 150 nm pores.

In addition, SZ_10d showed very high CO_2/CH_4 SFs (~238 at 50 °C) under dry conditions compared to those of other zeolite membranes (Fig. 5B) at a realistic biogas temperature of ~50-60 °C. This strongly indicates the reliable formation of the hybrid SZ membrane in this study. As observed for CO_2/N_2 separation, SZ_10d retained high CO_2/CH_4 SFs at 50 °C under wet conditions (~78 at H_2O vapor pressure of ~3 kPa and even higher value of ~145 at H_2O vapor pressure of ~12 kPa) (Fig. 5B). Fig. 5B clearly reveals that SZ_10d had good CO_2/CH_4 separation performance, comparable to those of other zeolite membranes, supporting the reliability of our synthetic approach in securing membrane hydrophobicity. Furthermore, to the best of our knowledge, SZ_10d shows the best CO_2/CH_4 separation performance under saturated water vapor pressure (~12 kPa) at ~50 °C. Nevertheless, the current CO_2 permeances through SZ_10d under wet conditions, which is relevant to the size of the membrane modules, should be increased by at least one order of magnitude for real applications. As inferred from the minor change in CO_2 permeance among SZ_*x*d (*x* = 6, 8, 10, and 12) in fig. S11F, the final permeance through the SZ membrane series would be significantly affected and limited by the support resistance. Thus, the next step toward practical use is to fabricate DDR@CHA hybrid membranes on high flux supports.

Conclusion

The concept of hetero-epitaxial growth was proven to be effective for the fabrication of a high-performance continuous zeolite membrane. Specifically, to the best of our knowledge, we, for the first time, have developed an alternative, reliable methodology to acquire CO_2 perm-selective DDR@CHA hybrid membranes. Unlike the conventional approach, the hetero-epitaxial growth of a SSZ-13 (CHA type zeolite) seed layer with a synthetic precursor that leads to the synthesis of DDR type zeolite phase allowed the formation of hybrid membranes with a major DDR phase in a reproducible manner. In particular, the structural compatibility between the CHA and DDR type zeolites is key to the growth of the hetero-epitaxial hybrid film. Desirably, the resulting hybrid films showed superior CO_2 perm-selectivities with respect to the both CO_2/N_2 and CO_2/CH_4 binary mixtures. Their surfaces were quite hydrophobic so that the high CO_2

perm-selectivities were well preserved in the wet feed. To the best of our knowledge, this performance was the best of those of previously reported zeolite membranes, especially with respect to the realistic wet feed. We are currently extending our current approach to fabricate other types of zeolite films to enrich the current membrane manufacturing protocol.

Acknowledgements

Funding: This work was financially supported by the Korea CCS R&D Center (KCRC) (2014M1A8A1049309), by the International Research & Development Program (2016K1A3A1A48954031), and by the Super Ultra Low Energy and Emission Vehicle (SULEEV) Center (2016R1A5A1009592) through National Research Foundation (NRF) of Korea. These three grants were funded by the Korea government (Ministry of Science and ICT). This research was also supported by Korea University Future Research Grant. SEM and XRD characterizations were conducted at the Korea University Engineering Laboratory Center, while TEM and partial SEM characterizations were carried out at the Korea Basic Science Institute (KBSI). FCOM images were obtained at the Korea Institute of Science and Technology (KIST). CO_2/N_2 and CO_2/CH_4 permeation measurements were carried out in the Choi group at Korea University. **Author Contribution:** J.C. and Y.J. conceived the project. Y.J. conducted most experiments (film/membrane synthesis and characterization, permeation tests, and membrane performance evaluation). J.C. and Y.J. prepared for the manuscript with input from other co-authors. S.H. obtained FCOM results. E.J. and E.K. contributed to measuring CO_2 perm-selectivities. H.B. helped to conduct the TEM analysis. N.C. helped to obtain better quality FCOM results. A.C.K.Y. contributed to analyzing the permeation test results. **Competing interests:** The authors declare no competing interests. **Data and materials availability:** All data are available in the manuscript or the supplementary materials.

Supplementary Materials

Materials and Methods
Supplementary Text
Figs. S1 to S16
Table S1
References (47-68)

References and Notes

1. N. Y. Du *et al.*, Polymer nanosieve membranes for CO_2-capture applications. *Nat. Mater.* **10**, 372-375 (2011).
2. M. Zhao, A. I. Minett, A. T. Harris, A review of techno-economic models for the retrofitting of conventional pulverised-coal power plants for post-combustion capture (PCC) of CO_2. *Energy Environ. Sci.* **6**, 25-40 (2013).
3. J. Y. S. Lin, Molecular sieves for gas separation. *Science* **353**, 121-122 (2016).
4. S. G. Li, J. L. Falconer, R. D. Noble, Improved SAPO-34 membranes for CO_2/CH_4 separations. *Adv. Mater.* **18**, 2601-2603 (2006).
5. X. Zhu *et al.*, A superacid-catalyzed synthesis of porous membranes based on triazine frameworks for CO_2 separation. *J. Am. Chem. Soc.* **134**, 10478-10484 (2012).
6. H. B. Park *et al.*, Polymers with cavities tuned for fast selective transport of small molecules and ions. *Science* **318**, 254-258 (2007).
7. S. Chu, Carbon capture and sequestration. *Science* **325**, 1599-1599 (2009).
8. M. E. Davis, Ordered porous materials for emerging applications. *Nature* **417**, 813-821 (2002).
9. H. Q. Yang *et al.*, Progress in carbon dioxide separation and capture: a review. *J. Eviron. Sci.* **20**, 14-27 (2008).
10. M. A. Snyder, M. Tsapatsis, Hierarchical nanomanufacturing: from shaped zeolite nanoparticles to high-performance separation membranes. *Angew. Chem. Int. Edit.* **46**, 7560-7573 (2007).
11. Z. P. Lai *et al.*, Microstructural optimization of a zeolite membrane for organic vapor separation. *Science* **300**, 456-460 (2003).
12. H. Y. Jiang, B. Q. Zhang, Y. S. Lin, Y. D. Li, Synthesis of zeolite membranes. *Chin. Sci. Bull.* **49**, 2547-2554 (2004).
13. N. Kosinov *et al.*, High flux high-silica SSZ-13 membrane for CO_2 separation. *J. Mater. Chem. A* **2**, 13083-13092 (2014).
14. E. Kim *et al.*, An Oriented, siliceous Deca-dodecasil 3R (DDR) zeolite film for effective carbon capture: insight into its hydrophobic effect. *J. Mater. Chem. A* **5**, 11246-11254 (2017).
15. X. H. Gu, J. H. Dong, T. M. Nenoff, Synthesis of defect-free FAU-type zeolite membranes and separation for dry and moist CO_2/N_2 mixtures. *Ind. Eng. Chem. Res.* **44**, 937-944 (2005).
16. J. Choi, S. Ghosh, Z. P. Lai, M. Tsapatsis, Uniformly a-oriented MFI zeolite films by secondary growth. *Angew. Chem. Int. Edit.* **45**, 1154-1158 (2006).
17. T. Tomita, K. Nakayama, H. Sakai, Gas separation characteristics of DDR type zeolite membrane. *Microporous Mesoporous Mater.* **68**, 71-75 (2004).
18. S. W. Yang *et al.*, DDR-type zeolite membrane synthesis, modification and gas permeation studies. *J. Membr. Sci.* **505**, 194-204 (2016).
19. M. J. den Exter, J. C. Jansen, H. van Bekkum, *Separation of permanet gases on the all-Silica 8-ring clathrasil DD3R*. J. Weitkamp, H. G. Karge, H. Pfeifer, W. Holderich, Eds., Zeolites and Related Microporous Materials: State of the Art 1994 (Elsevier Science Publ B V, Amsterdam, 1994), vol. 84, pp. 1159-1166.
20. F. Y. Zheng, W. H. Jing, X. H. Gu, N. P. Xu, J. H. Dong, Rapid synthesis of pure DD3R zeolite using ball-milled Sigma-1 seeds under static conditions. *J. Membr. Sci.* **48**, 6286-6292 (2013).
21. J. Gascon *et al.*, Accelerated synthesis of all-silica DD3R and Its performance in the separation of propylene/propane mixtures. *Microporous Mesoporous Mater.* **115**, 585-593 (2008).
22. M. Sen, A. Bose, P. Pal, J. K. Das, N. Das, Rapid synthesis of DDR zeolite at room temperature. *J. Am. Ceram. Soc.* **97**, 52-55 (2014).
23. E. Kim, W. X. Cai, H. Baik, J. Nam, J. Choi, Synthesis and sonication-induced assembly of Si-DDR particles for close-packed oriented layers. *Chem. Commun.* **49**, 7418-7420 (2013).
24. M. Mubashir, Y. F. Yeong, N. Nazri, K. K. Lau, Accelerated synthesis of Deca-dodecasil 3 rhombohedral (DDR3) zeolite crystals via hydrothermal growth coupled with ultrasonic irradiation method. *RSC Adv.* **5**, 22658-22664

(2015).
25. C. Gucuyener *et al.*, Facile synthesis of the DD3R zeolite: performance in the adsorptive separation of buta-1,3-diene and but-2-ene Isomers. *J. Mater. Chem.* **21**, 18386-18397 (2011).
26. A. W. Burton, G. S. Lee, S. I. Zones, Phase selectivity in the syntheses of cage-based zeolite structures: an investigation of thermodynamic interactions between zeolite hosts and structure directing agents by molecular modeling. *Microporous Mesoporous Mater.* **90**, 129-144 (2006).
27. Y. Bouizi, L. Rouleau, V. P. Valtchev, Factors controlling the formation of core-shell zeolite-zeolite composites. *Chem. Mat.* **18**, 4959-4966 (2006).
28. T. Wakihara, S. Yamakita, K. Iezumi, T. Okubo, Heteroepitaxial growth of a zeolite film with a patterned surface-texture. *J. Am. Chem. Soc.* **125**, 12388-12389 (2003).
29. A. M. Goossens, B. H. Wouters, V. Buschmann, J. A. Martens, Oriented FAU zeolite films on micrometer-sized EMT crystals. *Adv. Mater.* **11**, 561-564 (1999).
30. H. K. Jeong, J. Krohn, K. Sujaoti, M. Tsapatsis, Oriented molecular sieve membranes by heteroepitaxial growth. *J. Am. Chem. Soc.* **124**, 12966-12968 (2002).
31. T. Okubo *et al.*, Heteroepitaxial growth of a zeolite. *Angew. Chem. Int. Edit.* **40**, 1069-1071 (2001).
32. Z. Y. Wang *et al.*, Epitaxial growth of core-shell zeolite X-A composites. *Crystengcomm* **14**, 2204-2212 (2012).
33. A. S. Huang, N. Y. Wang, J. Caro, Stepwise synthesis of sandwich-structured composite zeolite membranes with enhanced separation selectivity. *Chem. Commun.* **48**, 3542-3544 (2012).
34. Y. Y. Xu, X. L. Wei, S. Liang, Y. L. Sun, Z. S. Chao, Synthesis of a ZSM-5/NaA hybrid zeolite membrane using kaolin as a modification layer. *New J. Chem.* **42**, 6664-6672 (2018).
35. E. Kim *et al.*, Mono-dispersed DDR zeolite particles by seeded growth and their CO_2, N_2, and H_2O adsorption properties. *Chem. Eng. J.* **306**, 876-888 (2016).
36. M. P. Bernal, J. Coronas, M. Menendez, J. Santamaria, Separation of CO_2/N_2 mixtures using MFI-type zeolite membranes. *AIChE J.* **50**, 127-135 (2004).
37. D. Singh, E. Croiset, P. L. Douglas, M. A. Douglas, Techno-economic study of CO_2 capture from an existing coal-fired power plant: MEA scrubbing vs. O_2/CO_2 recycle combustion. *Energy Convers. Manag.* **44**, 3073-3091 (2003).
38. T. C. Merkel, H. Q. Lin, X. T. Wei, R. Baker, Power plant post-combustion carbon dioxide capture: an opportunity for membranes. *J. Membr. Sci.* **359**, 126-139 (2010).
39. E. Ryckebosch, M. Drouillon, H. Veruaeren, Techniques for transformation of biogas to biomethane. *Biomass Bioenergy* **35**, 1633-1645 (2011).
40. P. Weiland, Biogas production: current state and perspectives. *Appl. Microbiol. Biotechnol.* **85**, 849-860 (2010).
41. J. Choi *et al.*, Grain boundary defect elimination in a zeolite membrane by rapid thermal processing. *Science* **325**, 590-593 (2009).
42. S. Hong *et al.*, Healing of microdefects in SSZ-13 membranes via filling with dye molecules and its effect on dry and wet CO_2 separations. *Chem. Mater.* **30**, 3346-3358 (2018).
43. G. Bonilla, M. Tsapatsis, D. G. Vlachos, G. Xomeritakis, Fluorescence confocal optical microscopy imaging of the grain boundary structure of zeolite MFI membranes made by secondary (seeded) growth. *J. Membr. Sci.* **182**, 103-109 (2001).
44. E. Kim *et al.*, Chemical vapor deposition on Chabazite (CHA) zeolite membranes for effective post-combustion CO_2 capture. *Environ. Sci. Technol.* **48**, 14828-14836 (2014).
45. Y. Chen, Y. T. Zhang, C. Zhang, J. Jiang, X. H. Gu, Fabrication of High-Flux SAPO-34 Membrane on Alpha-Al_2O_3 Four-Channel Hollow Fibers for CO_2 Capture from CH_4. *J. CO_2 Util.* **18**, 30-40 (2017).
46. L. Wang *et al.*, Preparation of defect-free DDR zeolite membranes by eliminating template with ozone at low temperature. *J. Membr. Sci.* **539**, 152-160 (2017).

Supplementary Materials

A hetero-epitaxially grown zeolite film and its unprecedented use as a perm-selective membrane

Yanghwan Jeong,[1] Sungwon Hong,[1] Eunhee Jang,[1] Eunjoo Kim,[1]

Hionsuck Baik,[2] Nakwon Choi,[3] Alex C.K. Yip,[4] and Jungkyu Choi[1,*]

[1] Department of Chemical & Biological Engineering, College of Engineering, Korea University, 145 Anam-ro, Seongbuk-gu, Seoul 02841, Republic of Korea

[2] Korea Basic Science Institute (KBSI), Seoul Center, 145 Anam-ro, Seongbuk-gu, Seoul 02841, Republic of Korea

[3] Center for BioMicrosystems, Brain Science Institute, Korea Institute of Science and Technology (KIST), Hwarang-ro 14-gil, Seongbuk-gu, Seoul 02792, Republic of Korea

[4] Chemical and Process Engineering, University of Canterbury, Private Bag 4800, Christchurch, New Zealand

* Corresponding Author

E-mail address: jungkyu_choi@korea.ac.kr, Phone: +82-2-3290-4854, and Fax: +82-2-926-6102

S1. Materials and Methods

S1.1. Synthesis of SSZ-13 (CHA) particles

SSZ-13 seed particles were synthesized by modifying a previously reported method (*47, 48*). The bimodal particle size distribution of the resulting SSZ-13 particles (~0.7 μm and ~5 μm), as well as their larger sizes, prevented their use as seed particles, which should be monodisperse and small enough to form a uniform seed layer. In this study, a modified synthesis method, where the molar composition of deionized (DI) water was reduced, led to the synthesis of small (~230 nm), monodisperse SSZ-13 particles.

Specifically, *N*, *N*, *N*-trimethyl-1-adamantylammonium hydroxide (TMAdaOH, 25%, SACHEM) was first added to DI water in a polypropylene bottle. Then, sodium hydroxide was added to the above solution (≥98% pellets, Sigma-Aldrich). The resulting mixture was further homogenized for ~20 min using a shaker machine (JeioTech, Si-300R). After that, a silica source, LUDOX® HS-40 colloidal silica (40 wt% suspension in H_2O, Sigma-Aldrich), was added dropwise to the homogenized solution while stirring the mixture. Finally, aluminum hydroxide (reagent grade, Sigma-Aldrich) was dissolved in the mixture. The resulting mixture was further stirred at room temperature for ~2 d. The final molar composition of the synthetic mixture was 100 SiO_2: 20 NaOH: 5 $Al(OH)_3$: 20 TMAdaOH: 1600 H_2O; the original content of DI water in the literature was 4400 (*47*). The prepared synthetic precursor was then transferred into a Teflon liner (45 mL) and the liner was inserted into a stainless-steel autoclave. The autoclave was moved to a preheated oven (Pluskolab, PL_HV_250) at 160 ℃ and rotated at ~45 rpm. After 7 d, synthesis was stopped by quenching the autoclave with tap water. Then, the solid products were recovered by repeating a series of (i) centrifugation (centrifuge; Hanil Science Industrial, Combi-514R), (ii) decanting, and (iii) re-dispersion with DI water five times. The recovered particles were dried in a drying oven (Pluskolab, HB-502M) at 70 ℃ and further calcined at 550 ℃ for 12 h at a ramp rate of 1 ℃·min^{-1} under air flow (200 mL·min^{-1}) in a furnace (Pluskolab, CRF-M20-UP).

S1.2. SSZ-13 (CHA) seed layer formation

About 0.03 g of the calcined SSZ-13 seed particles was added to 40 mL of ethanol to prepare a seed suspension. This suspension was sonicated (JeioTech, UC-10) for 20 min to yield a homogeneously dispersed solution in the conical centrifuge tube (50 mL capacity; Falcon); this was poured into a petri dish. Subsequently, the polished side of an α-Al_2O_3 disc was placed in contact with the seed suspension for 30 s. Subsequently, the α-Al_2O_3 disc was lifted slowly away, sweeping up the surface of the suspension, and the disc was dried for 30 s under ambient conditions. This dip-coating process was repeated four times to ensure full surface coverage. The seed-coated α-Al_2O_3 disc was calcined at 450 ℃ for 4 h at a ramp rate of 1 ℃·min^{-1} in the furnace.

S1.3. DDR@CHA membrane fabrication

S1.3.1. Synthesis of the structure directing agent (SDA), methyltropinium iodide

Methyltropinium iodide (MTI) is a known SDA for the synthesis of ZSM-58 (DDR type zeolite) (*49*). In this study, MTI was prepared by the methylation of tropine (98%, Alfa Aesar) with iodomethane (99%, Sigma-Aldrich). For this reaction, 200 mL of ethanol was first poured into a 500 mL round-bottomed flask, which was connected to a reflux condenser. Next, 50 g of tropine was dissolved in ethanol while stirring with a magnetic bar. Prior to the reaction, the flask was wrapped with aluminum foil to establish a dark environment and argon was fed to the flask to secure an inert environment. Then, 51 g of iodomethane was added dropwise to the flask while stirring with a magnetic bar. After completing the addition, the reaction was carried out at room temperature for 3 d. During reaction, the solution was continuously stirred using the magnetic bar and the flask was sealed with Teflon tape to preserve the inert conditions. The products formed as a white powder and were filtered by vacuum filtration, and washed with copious amounts of ethanol to achieve high purity. The recovered solid powder was further dried in the oven at 70 ℃ for ~1 d before use.

S1.3.2. Secondary growth of ZSM-58 zeolites on the SSZ-13 seed layer

The secondary growth of the SSZ-13 seed layer was carried out with a synthetic precursor that led to the synthesis of all-silica ZSM-58 zeolites. First, MTI was dissolved in DI water. For homogenization, the polypropylene bottle was sonicated for 20 min. Subsequently, a silica source (here, LUDOX® HS-40 colloidal silica; 40 wt% suspension in H_2O, Sigma-Aldrich) was quickly added to the aqueous MTI solution. The solution was well mixed with the shaker machine for ~12 h. For convenience, this solution is referred to as solution A. At the same time, a certain amount of sodium hydroxide (≥ 98% pellets, Sigma-Aldrich) was dissolved in DI water and further mixed by the shaker machine for ~12 h. This solution is referred to as solution B. The prepared A and B solution were then mixed and further shaken for ~12 h until the opaque mixture, observed right after mixing, became a transparent solution. The final molar composition of the synthetic solution was 70 SiO_2: 23 NaOH: 17.5 MTI: 2800 H_2O. The molar ratio of DI water for the synthetic precursor of ZSM-58 was 1 solution A: 4 solution B.

About 30 mL of the prepared synthetic solution was poured into the Teflon liner (45 mL), which contained the seed-coated α-Al_2O_3 disc. The seeded-coated side of an α-Al_2O_3 disc was placed at a tilted angle with the help of a Teflon holder while facing downward. The disc-containing Teflon liner was placed in the stainless-steel autoclave and the autoclave was moved to the oven, which had been preheated to 130 ℃. The reaction was conducted under static conditions. The hydrothermal secondary growth process was carried out for different periods (4, 6, 8, 10, and 12 d). At the end of the reaction, the autoclave was taken out and rapidly quenched with tap water. After taking out the disc sample, the synthesized membrane was washed with ample DI water and further dried in an oven (HYSC, DO-42) at 100 ℃. Finally, the dried membrane sample was thermally activated by calcination at 550 ℃ for 12 h in the furnace under an air flow of 200 mL·min^{-1}. For calcination in this study, a slow calcination program at a ramp rate of 0.2 ℃·min^{-1} was adopted in an effort to minimize the formation of cracks in the membrane samples. For convenience, the calcined zeolite membrane is referred to as SZ_*x*d, where S stands for a

SSZ-13 seed layer, Z represents the ZSM-58 portion after secondary growth, and *x* indicates the hydrothermal secondary growth time in days.

S1.4. Secondary growth of a DDR seed layer with a CHA zeolite synthetic precursor

In fig. S5, A and B, SEM images show that the DDR seed layer was uniformly formed. Conventional, diamond-shaped all-silica DDR particles with a size of 820 ± 150 nm were synthesized and deposited on an α-Al_2O_3 disc following a previously reported method (*50*). The corresponding XRD pattern of the DDR seed layer in fig. S5E confirms that the formed seed layer had a pure DDR zeolite phase. In addition, the SEM images and XRD pattern of the DDR seed layer after conducting secondary growth with a SSZ-13 synthetic precursor for 6 d are shown in fig. S5, C to E. The final molar composition of the SSZ-13 (Si/Al = 20) synthetic precursor, which was used for the secondary growth of the DDR seed layer, was 20 NaOH: 5 $Al(OH)_3$: 100 SiO_2: 20 TMAdaOH: 8800 H_2O and the hydrothermal reaction was carried out at 160 °C for 6 d. After completing the reaction, the membrane sample was also calcined at 550 °C for 12 h at a ramp rate of 0.2 °C·min^{-1} in the furnace under an air flow of 200 mL·min^{-1}. The SEM images show that the SSZ-13 film had formed a continuous layer on top of the DDR seed layer (fig. S5, C and D). In addition, the XRD peaks corresponding to the CHA zeolite are clearly visible after 6-d hydrothermal reaction in the XRD pattern (fig. S5E); the XRD pattern of the CHA@DDR membrane still contained the (101) peak of XRD pattern of the DDR seed layer (DDR type zeolite) in the magnified XRD pattern in the 2 θ range from 5° to 8.5°.

S1.5. Characterization

Scanning electron microscopy (SEM) images were acquired from Pt-coated samples by using field emission-scanning electron microscopy (FE-SEM, Hitachi S-4300). For Pt coating, a sample was sputtered with Pt (generated at 30 mA) for 30 s using a Hitachi E-1045 ion sputter. In addition, energy dispersive X-ray spectroscopy (EDX) results were obtained using a Hitachi S-4800 FE-SEM. A cross-sectioned membrane sample was first prepared by using a dual beam-focused ion beam (DB-FIB) of

TESCAN LYRA3 XMH SEM. Before conducting FIB, the sample was coated with carbon and Pt layers to prevent any damage by the beam. Then, FIB with Ga ions thinned the thickness of cross-sectioned parts to ~100 nm to be suitable for transmission electron microscopy (TEM) analysis. Then, the prepared cross-sectioned samples were used to obtain the cross-sectional view TEM images, and scanning transmission electron microscopy (STEM) images and the diffraction patterns of the CHA and DDR type zeolite parts in the STEM microprobe mode. For this purpose, we used an FEI XFEG-Titan themis^3 Double Cs & Mono. TEM. For clarity, in this study, if the zone axis and Miller index contained two digits, they were described in the blank space between the numbers. X-ray diffraction (XRD) patterns were acquired with a Rigaku Model D/Max-2500V/PC diffractometer with Cu K_α radiation (λ = 0.154 nm). To compare the XRD results, simulated XRD patterns of all-silica CHA and DDR zeolites were prepared from their crystallographic information files (CIFs) through the Mercury software (Cambridge Crystallographic Data Centre; CCDC). The CIFs of all-silica CHA and DDR zeolites were downloaded from the International Zeolite Association (IZA) website (http://www.iza-online.org). Crystallographic preferential orientation (CPO) values were obtained by analyzing the XRD patterns of the powder and membrane samples following a previously described method (*51*). In addition, to evaluate the hydrophobicity of the membrane sample, the contact angles of water droplets on the membrane surfaces were measured using a SEO Phoenix-300 contact angle analyzer.

The separation performance tests of the SZ membrane series were carried out in the Wicke-Kallenbach mode, for which a total pressure in both feed and permeate sides were maintained at 1 atm. In the feed, the partial pressures of CO_2:N_2 or CO_2:CH_4 binary mixtures were 50.5 kPa:50.5 kPa under dry conditions (referred to as Dry CO_2:N_2=50:50 or Dry CO_2:CH_4=50:50). In addition, under wet conditions, the partial pressures of the binary components (CO_2:N_2 or CO_2:CH_4) were 49 kPa each along with an additional 3 kPa of H_2O vapor (referred to as Wet CO_2:N_2=50:50 or Wet CO_2:CH_4=50:50). Furthermore, for the simulated flue gas from a coal-fired power plant (*52-54*), feeds with (i) 15.2 kPa CO_2: 85.8 kPa N_2 under dry conditions (referred to as Dry CO_2:N_2=15:85) and (ii) 14.7 kPa CO_2: 83.3 kPa N_2: 3 kPa H_2O

vapor under wet conditions (referred to as Wet CO_2:N_2=15:85) were used. Finally, feed gas mixtures of (i) 5 kPa CO_2: 96 kPa N_2 under dry conditions (referred to as Dry CO_2:N_2=5:95) and (ii) 4.9 kPa CO_2: 93.1 kPa N_2: 3 kPa H_2O vapor under wet conditions (referred to as Wet CO_2:N_2=5:95) were used in an effort to simulate the flue gas from a gas-fired power plant (*55-58*). The total flow rates of the both feed (dry basis) and sweep (helium) gas streams were 100 mL·min^{-1}. The permeating gas in the permeate side was continuously carried with the sweep gas into a gas chromatograph (GC, Young Lin (YL) 6100 GC system for CO_2/N_2 analysis and a YL 6500 GC system for CO_2/CH_4 analysis) equipped with a thermal conductivity detector (TCD) for CO_2/N_2 and a pulsed discharge ionization detector (PDD) for CO_2/CH_4. In particular, CH_4 and H_2 (~5 mL·min^{-1}) were added to the permeating gas sweep streams, because they were used as internal standards for the reliable estimation of the permeation rates of CO_2/N_2 and CO_2/CH_4 binary mixtures, respectively.

Fluorescent confocal optical microscopy (FCOM) analysis (*59*) of SZ_*x*d was performed to investigate the defective structure hidden in the membranes using a ZEISS LSM 700 confocal microscope with a solid-state laser (555 nm wavelength). Fluorescein sodium salt (Sigma-Aldrich) was used as the dye molecule and has a molecular size of ~1 nm (*60*), which is larger than the pore size of a DDR type zeolite (0.36 × 0.43 nm^2) but comparable to or smaller than the size of the defects. For preparation, membrane samples were dyed by placing them in contact with 1 mM fluorescein sodium salt solutions. In particular, the membrane surface was placed in contact with the dye solutions for 4 d using an osmosis type module (*61*). After completing the dyeing process, the FCOM images of the dyed SZ_*x*d samples were obtained along the membrane thickness from the membrane surface to the interface between the membrane and the α-Al_2O_3 support.

S2. Supplemental results and discussion

S2.1. Secondary growth of a DDR seed layer with a CHA zeolite synthetic precursor

We considered the opposite sequence in the hetero-epitaxial growth, i.e., film growth of CHA zeolites from a DDR seed layer. For this, a DDR seed layer was first formed with the use of diamond-shaped DDR particles as seeds (fig. S5, A and B, and S5E) (*62*). Despite the low degree of *c*-out-of-plane oriented DDR particles in the seed layer, a continuous hybrid film of CHA@DDR constituents was well formed (fig. S5, C to E), indicating the reliable hetero-epitaxial growth based on the structural compatibility of the pair of zeolites. Nevertheless, the insufficient number of *c*-out-of-plane oriented DDR particles likely prevented the effective inter-growth toward a continuous film (*63*), as reflected by the blossoming flower-like crystal grains (fig. S5, C and D) seemingly arising from the lack of proper nuclei (*64, 65*). In contrast, a randomly oriented SSZ-13 seed layer in this study was effective for growing heterogeneous DDR zeolites along the *c*-axis, because the *c*-axis in these SSZ-13 particles was more likely to be positioned in the out-of-plane direction.

S2.2. Secondary growth of a CHA seed layer with a MFI zeolite synthetic precursor

Along with the successful demonstration of the hetero-epitaxial growth of DDR and CHA type zeolites irrespective of growth sequence, we further explored if the growth of MFI type zeolites from the SSZ-13 seed layer was also feasible. This would support the conclusions drawn from the current results. Indeed, a continuous film was not synthesized by using two synthetic precursor compositions that are commonly used for the facile crystal growth of MFI zeolites (fig. S6, A and B). Unlike the 8-MR CHA zeolite, the 10-MR MFI zeolite crystallizes in the orthorhombic crystal system and the corresponding space group is *Pnma* ($a \neq b \neq c$ with $\alpha = 90°$, $\beta = 90°$, and $\gamma = 90°$). Furthermore, the unit cell dimensions of the CHA and MFI zeolites are different (CHA type zeolites, *a*: 13.6750 Å, *b*: 13.6750 Å, and *c*: 14.7670 Å vs. MFI type zeolites, *a*: 20.0900 Å, *b*: 19.7380 Å, and *c*: 13.1420 Å). This example of the

failure of hetero-epitaxial growth strongly supports the importance of the structural compatibility between two types of zeolites to achieve a heterogeneous zeolite film.

S2.3. Membrane properties of the membrane SZ series

To understand the membrane properties as a function of secondary growth time in the range of 4 to 12 d, top view and cross-sectional view SEM images of SZ membranes, along with contact angle measurements of water droplets, were obtained (fig. S7). The top view SEM images (fig. S7, A to E) of the SZ membrane series show that as the secondary growth time increased, the surface became gradually denser, along with a concomitant increase in the grain size. The cross-sectional view SEM images (fig. S7, F to J) clearly reveal that the thickness of the SZ membrane series monotonically increased with increasing secondary growth time (for example, 2.8 ± 0.3 μm for SZ_4d vs. 7.0 ± 0.3 μm for SZ_10d). It was noted that as the thickness of SZ membrane increased, the corresponding hydrophobicity also increased (figs. S7, F to O, and S8) except in SZ_4d, which was likely discontinuous (figs. S7A and S8, A1 to A6). The thicknesses and contact angles of the water droplets for the SZ membrane series are summarized in table S1.

Apparently, as the secondary growth duration increased, the (101) peak intensity stemming from the SSZ-13 seed layer monotonically decreased, indicating the gradual growth of the ZSM-58 zeolite in the resulting hybrid film (fig. S9). Clearly, the magnified XRD patterns in the 2 θ range of 8-10° in the left column in fig. S9 confirm the decreasing amount of SSZ-13 particles in the DDR@CHA hybrid membranes. In fig. S10, we have plotted the crystallographic preferential orientation (CPO) values to demonstrate the preferred out-of-plane orientation of the SZ membrane series. Although not pronounced, an increase in secondary growth time favored the crystal growth in the *h0h*-plane orientation, which is similar to the gradual increase in the *h0h*-plane orientation in homogenous DDR membranes with time in our previous study (*50*).

S2.4. Permeation tests of membrane SZ_10d under different feed conditions

In addition to the equimolar CO_2/N_2 binary mixture, we carried out permeation tests of SZ_10d with respect to other CO_2/N_2 feed ratios (CO_2:N_2 = 15:85 and CO_2:N_2 = 5:95), which are similar to the flue gas streams from coal-fired (*52-54*) and natural gas-fired power plants (*55-58*), respectively (fig. S12). Notably, the permeation behaviors of CO_2 and N_2 molecules under both dry and wet conditions were comparable to those observed in Fig. 3, A and B, indicating the linear response of SZ_10d with respect to the change in the partial pressure of CO_2 and N_2 molecules. Specifically, the max CO_2/N_2 SFs under dry conditions were as high as 17.0 ± 1.0 for CO_2:N_2 = 15:85 (fig. S12A) and 20.0 ± 1.3 for CO_2:N_2 = 5:95 at 30 °C (fig. S12C) compared to 15.2 ± 0.4 for CO_2:N_2 = 50:50 (Fig. 3A). We found that the max CO_2/N_2 SFs gradually increased with decreasing partial pressure of CO_2 molecules as a result of the slightly increased CO_2 permeance. This can be ascribed to the higher adsorption ability favoring CO_2, as reflected by the higher slope in the adsorption isotherm at a lower CO_2 partial pressure (*66, 67*). Similarly, under wet conditions, the CO_2/N_2 SFs at 50 °C, a representative flue gas temperature, were as high as 13.9 ± 1.3 for CO_2:N_2 = 15:85 (fig. S12B) and 16.5 ± 3.1 for CO_2:N_2 = 5:95 (fig. S12D).

In fig. S13, we summarize the molar fluxes and permeances of CO_2 and N_2 molecules along with the corresponding CO_2/N_2 SFs at 30 °C as a function of the molar composition of CO_2 molecules in the feed. The CO_2 partial pressure in the feed increased, but the CO_2 molar flux did not increase as much. Accordingly, the corresponding CO_2 permeance decreased monotonically under dry conditions (fig. S13, A and C). In contrast, the molar flux of N_2 molecules increased with increasing partial pressure, thus resulting in almost constant permeance of N_2 molecules under dry conditions (fig. S13, A and C). This can be ascribed to the above-mentioned higher adsorption behavior of CO_2 at the lower pressures, while the adsorption isotherm of N_2 was always linear, obeying the Henry's law up to 1 bar (*66*). Under wet conditions, the molar flux of CO_2 molecules, although lower than those under dry conditions, linearly increased with increasing partial pressure, thus resulting in the constant permeance of CO_2 molecules (fig.

S13, B and D). In contrast, the molar flux of N_2 molecules was almost constant, thus decreasing their permeances at the lower composition of CO_2 molecules and, concomitantly, increasing the CO_2/N_2 SF (fig. S13, B and D). Despite the varied CO_2/N_2 SFs at different concentrations of CO_2 molecules, it was noted that high CO_2/N_2 SFs (close to or larger than 10) could be achieved at a saturated water vapor pressure at 30 °C by using the hydrophobic SZ membrane.

Table S1. Thickness and contact angles of water droplets of the SZ membrane series.

Sample	Thickness (μm)	Contact angle of water droplet (°)
SZ_4d	2.8 ± 0.3	19
SZ_6d	4.3 ± 0.4	48
SZ_8d	6.0 ± 0.4	73
SZ_10d	7.0 ± 0.3	83
SZ_12d	7.8 ± 0.4	100

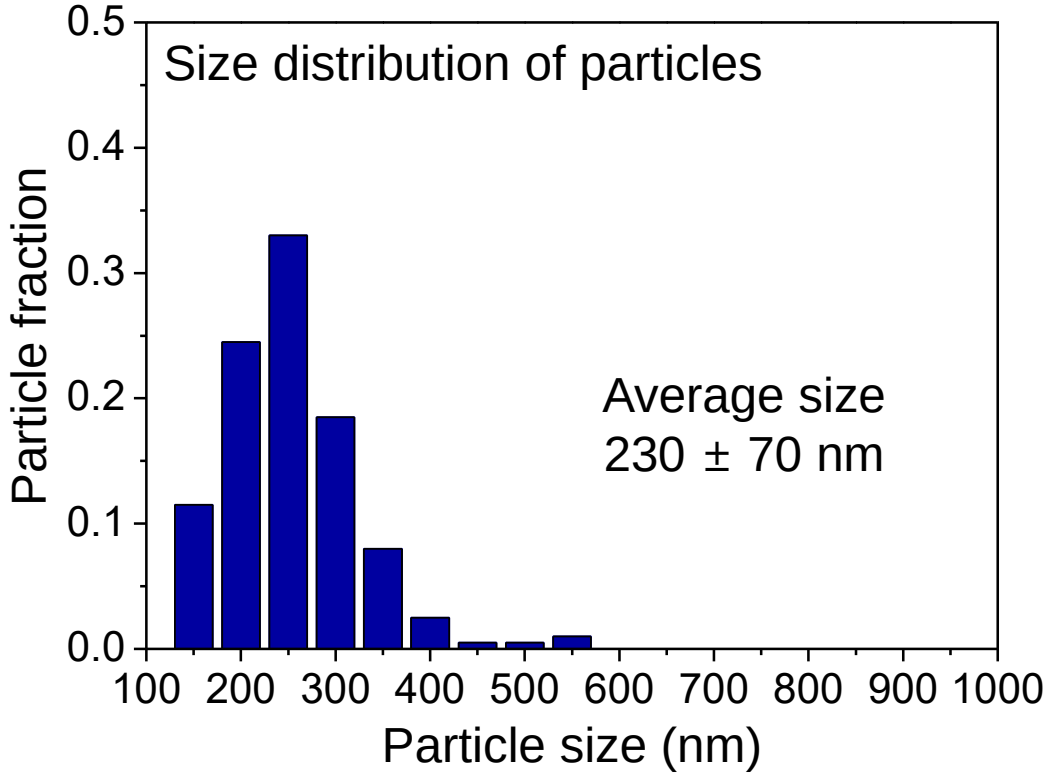

Fig. S1. Size distribution of the SSZ-13 seed particles used for formation of a seed layer shown in Fig. 1A. For estimation, the longest dimension of each particle was measured. The average size and its standard deviation were obtained from the measurement of more than 200 particles.

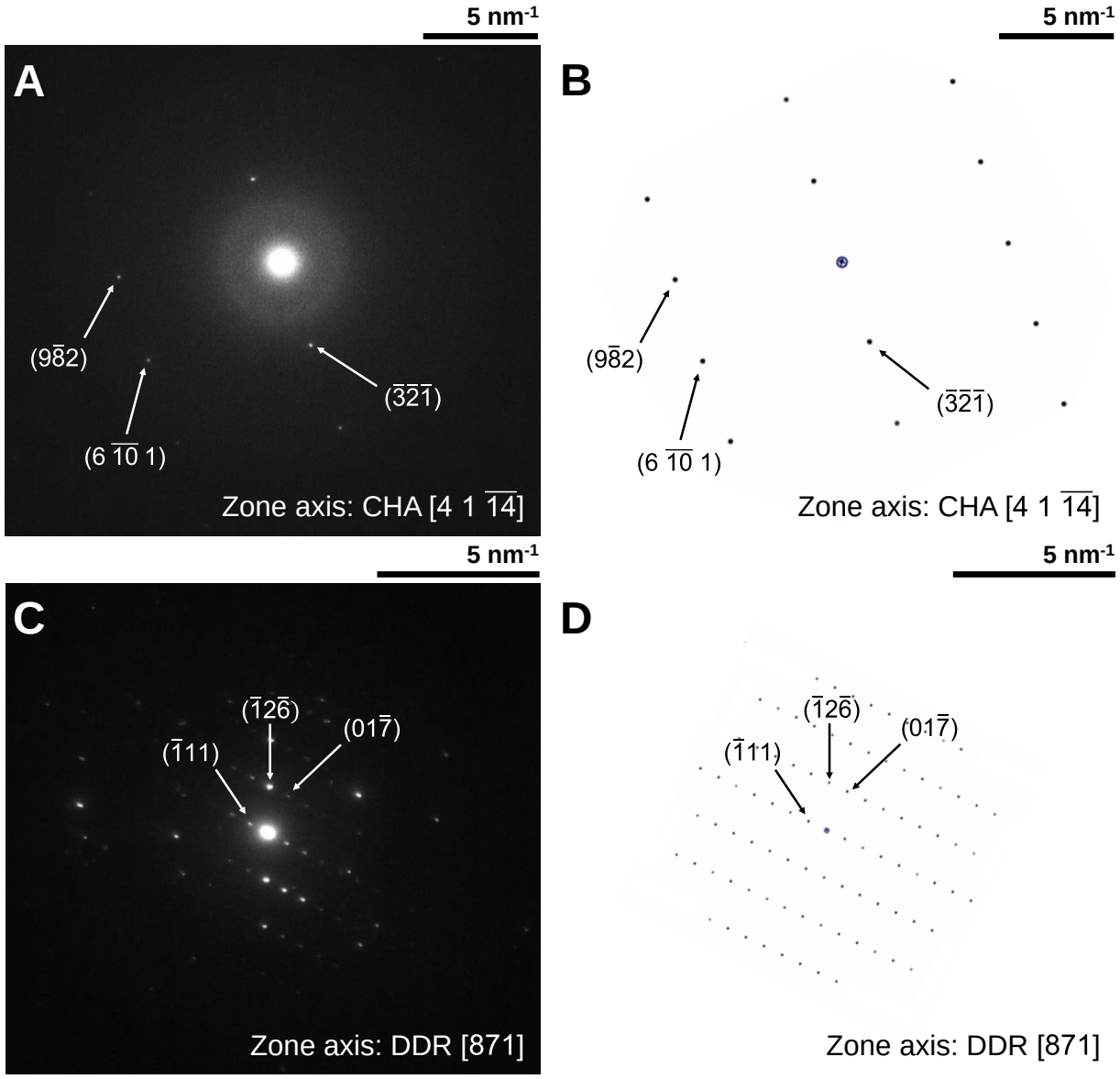

Fig. S2. Electron diffraction patterns of the hetero-epitaxially grown zeolite film along with the simulated patterns. (**A** and **C**) Experimental and (**B** and **D**) simulated electron diffraction patterns of CHA (Fig. 2E) and DDR (Fig. 2F) zeolite phases. For clarity, the experimental and simulated diffraction patterns are displayed side by side. The Miller indices are included on each electron diffraction pattern.

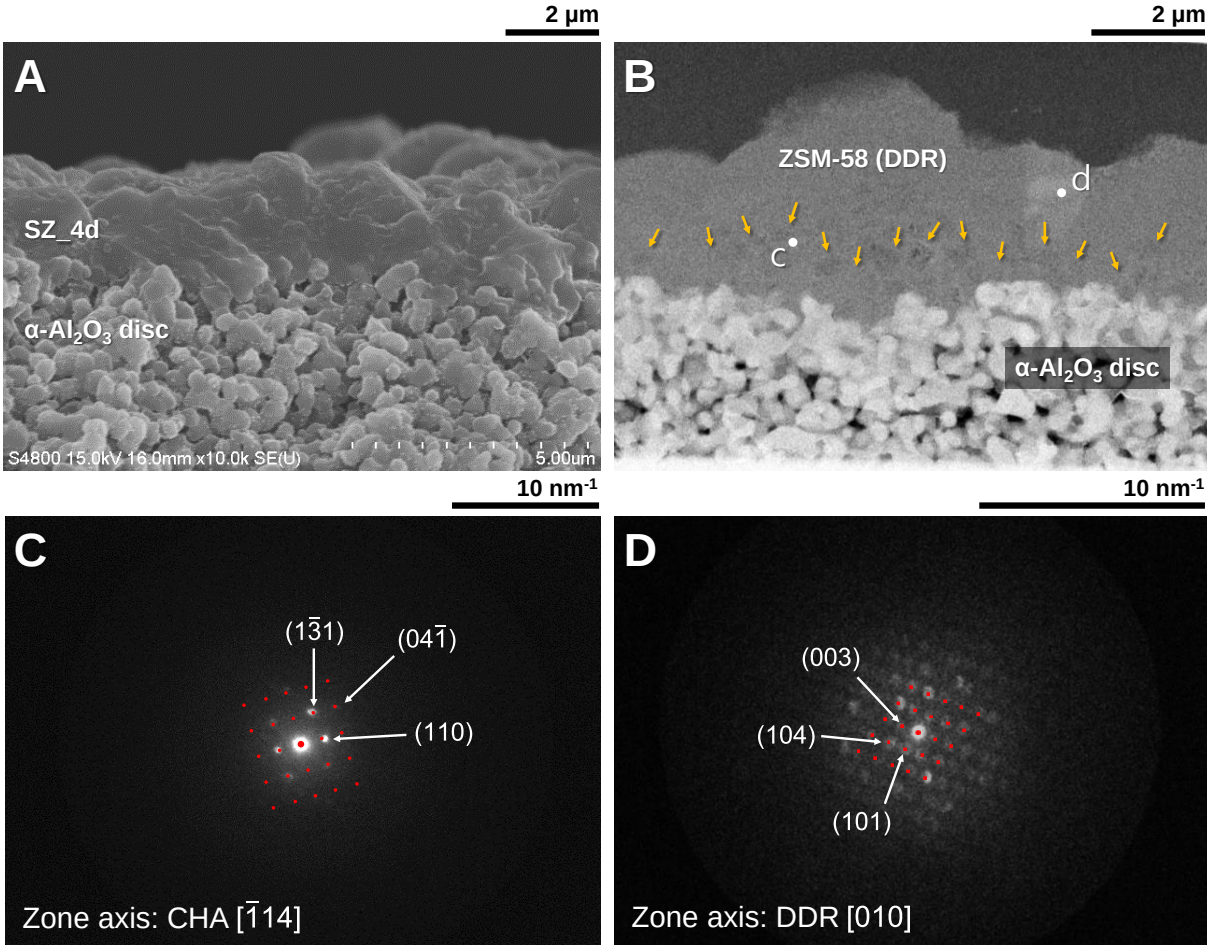

Fig. S3. Identification of the CHA and DDR zeolites in SZ_4d. Cross-sectional view (**A**) SEM and (**B**) STEM images of SZ_4d. In (B), orange arrows point to the SSZ-13 seed particles. Electron diffraction patterns obtained from the white dots labeled "C" and "D" in (B); the corresponding simulated patterns (red dots) are superimposed on the experimental patterns. The simulated diffraction patterns in (**C** and **D**) are obtained along the [$\bar{1}$14] zone axis in the CHA zeolite and the [010] zone axis in the DDR zeolites, respectively. In addition, the Miller indices are included on each diffraction pattern.

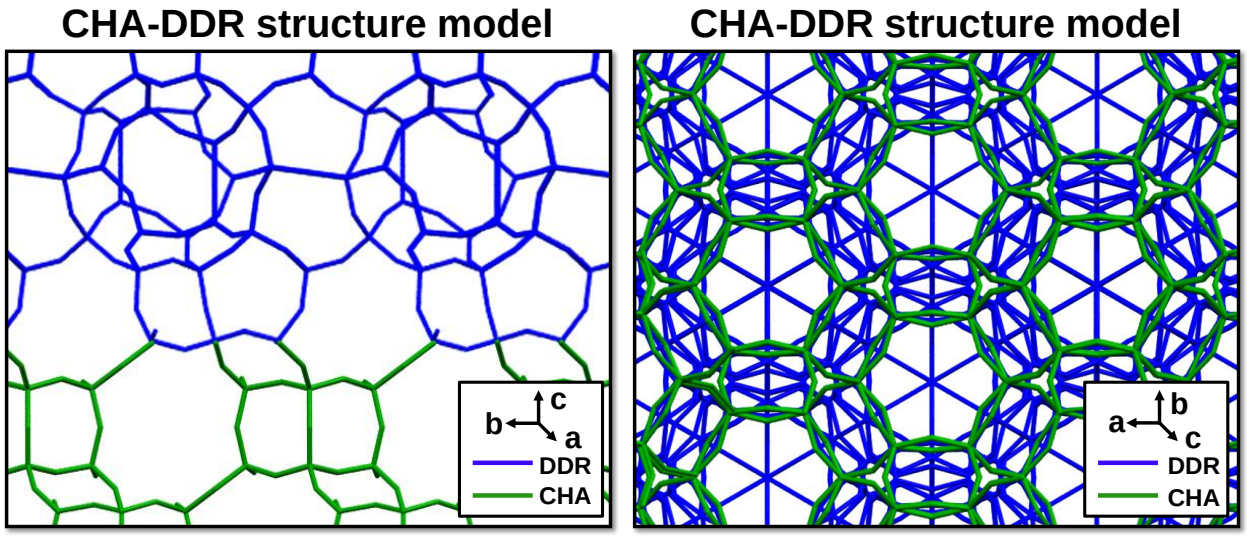

Fig. S4. Schematic structural model for plausible epitaxial growth of the DDR type zeolite from the CHA type zeolite at the interface. Blue and green structure models represent the DDR and CHA type zeolites, respectively. Side view (*left*) and top view (*right*) of a hetero-junction parts connected along the *c*-axis.

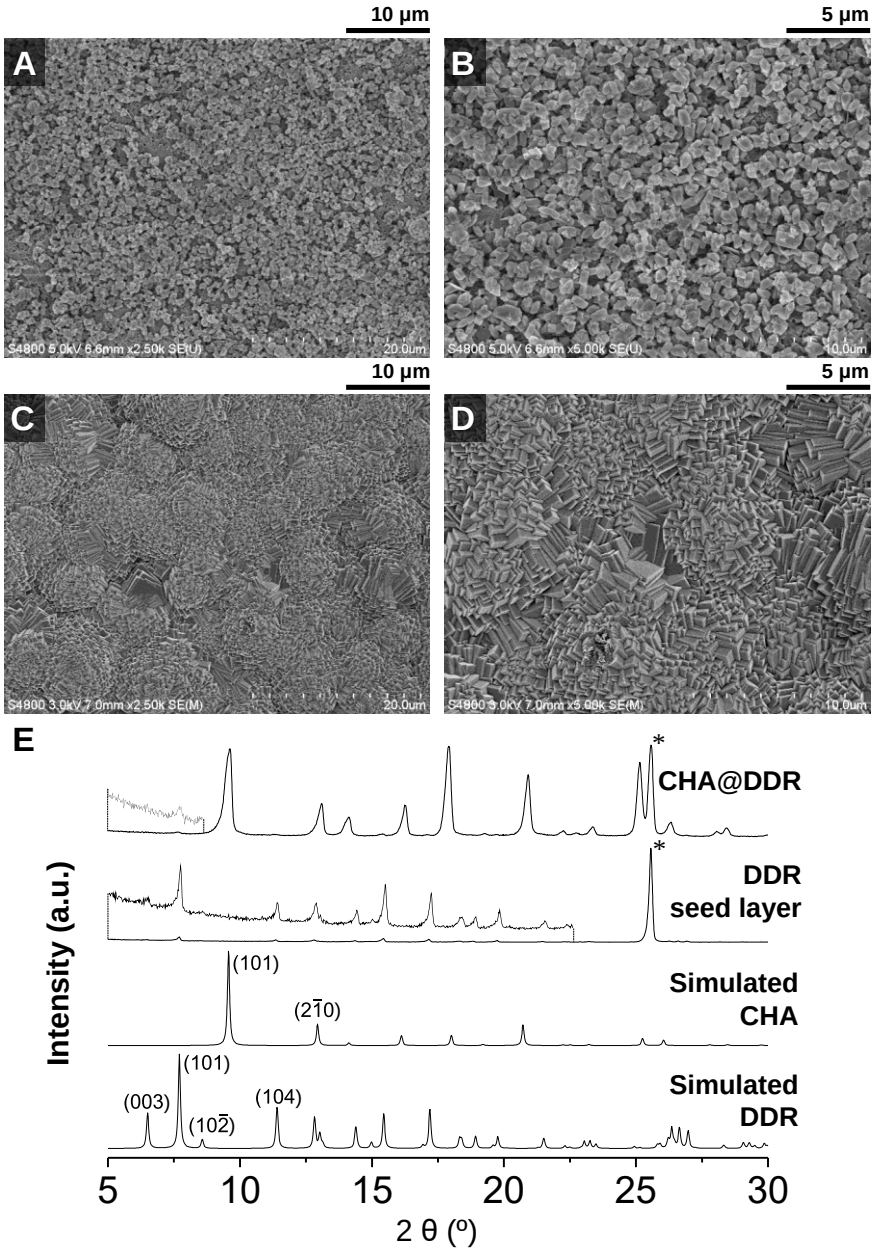

Fig. S5. SEM and XRD results of a DDR seed layer and its heteroepitaxial growth with a CHA synthetic precursor. (**A**) Low and (**B**) high magnification SEM images of an all-silica DDR seed layer formed on top of an α-Al_2O_3 disc and (**C**) low and (**D**) high magnification SEM images of a sample obtained after the secondary growth of the DDR seed layer shown in (A and B) using a SSZ-13 (CHA type zeolite, Si/Al = 20) zeolite synthetic precursor for 6 d. In addition, XRD patterns of (A and B) the DDR seed layer and (C and D) the CHA@DDR membrane are given in (**E**), along with the simulated XRD patterns of all-silica DDR and CHA zeolites. The asterisks (*) denote the XRD peaks from the α-Al_2O_3 disc.

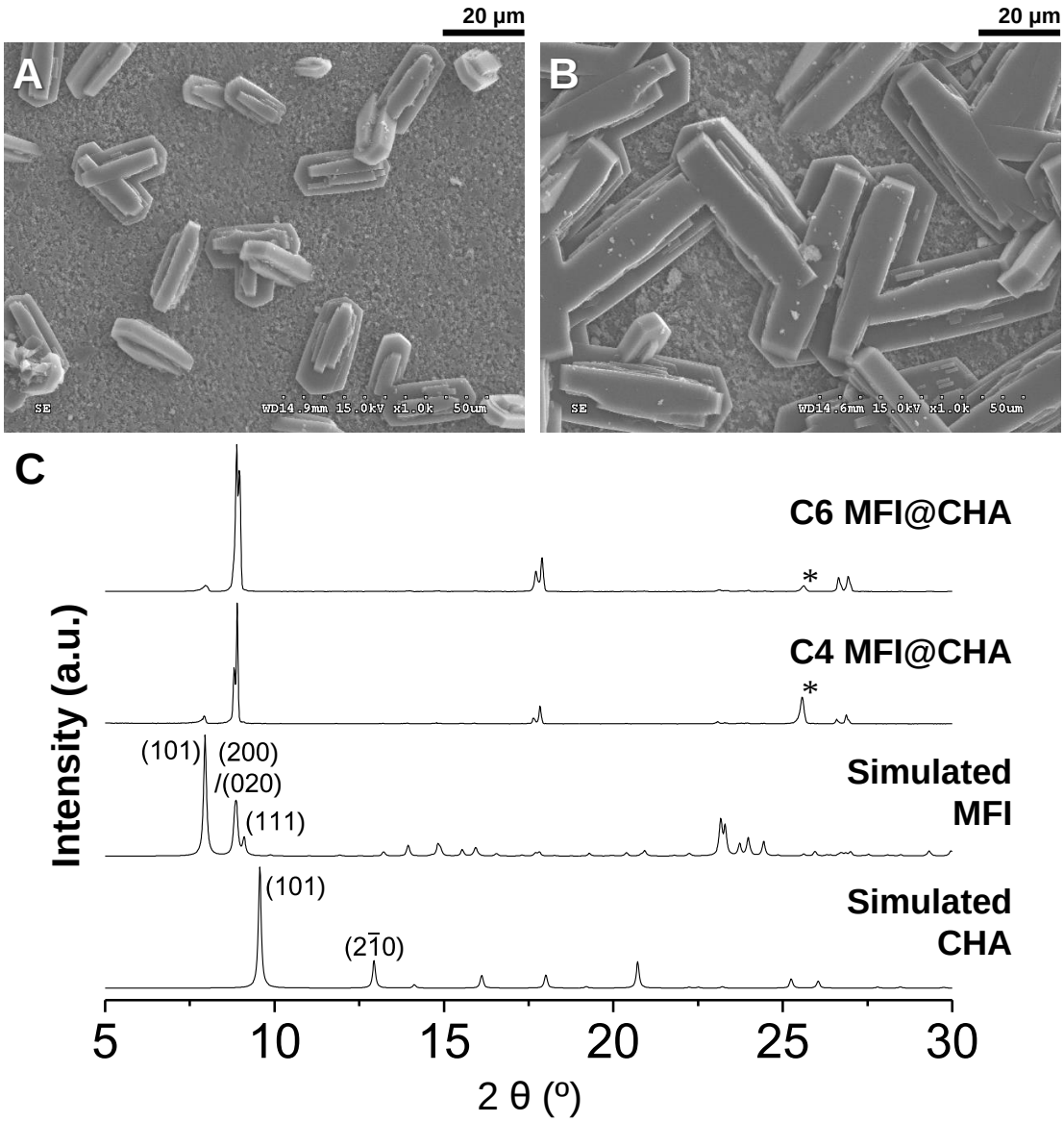

Fig. S6. SEM and XRD results of films grown from the SSZ-13 seed layer with MFI synthetic precursors. (**A** and **B**) Top view SEM images of SSZ-13 (CHA type zeolite) seed-coated α-Al_2O_3 discs after conducting secondary growth methodology with different MFI synthetic precursors. The final molar compositions and hydrothermal secondary growth conditions were 40 SiO_2: 9 TPAOH: 9500 H_2O: 160 EtOH at 175 °C for 1 d (adopted from the literature (*68*)) for (A) C4 MFI@CHA and 60 SiO_2: 9 TPAOH: 9500 H_2O: 240 EtOH at 175 °C for 2 d (adopted from the literature (*63*)) for (B) C6 MFI@CHA. In addition, XRD patterns of C4 MFI@CHA and C6 MFI@CHA membranes are given in (**C**) along with the simulated XRD patterns of all-silica CHA and MFI zeolites. The asterisks (*) denote the XRD peaks from the α-Al_2O_3 disc.

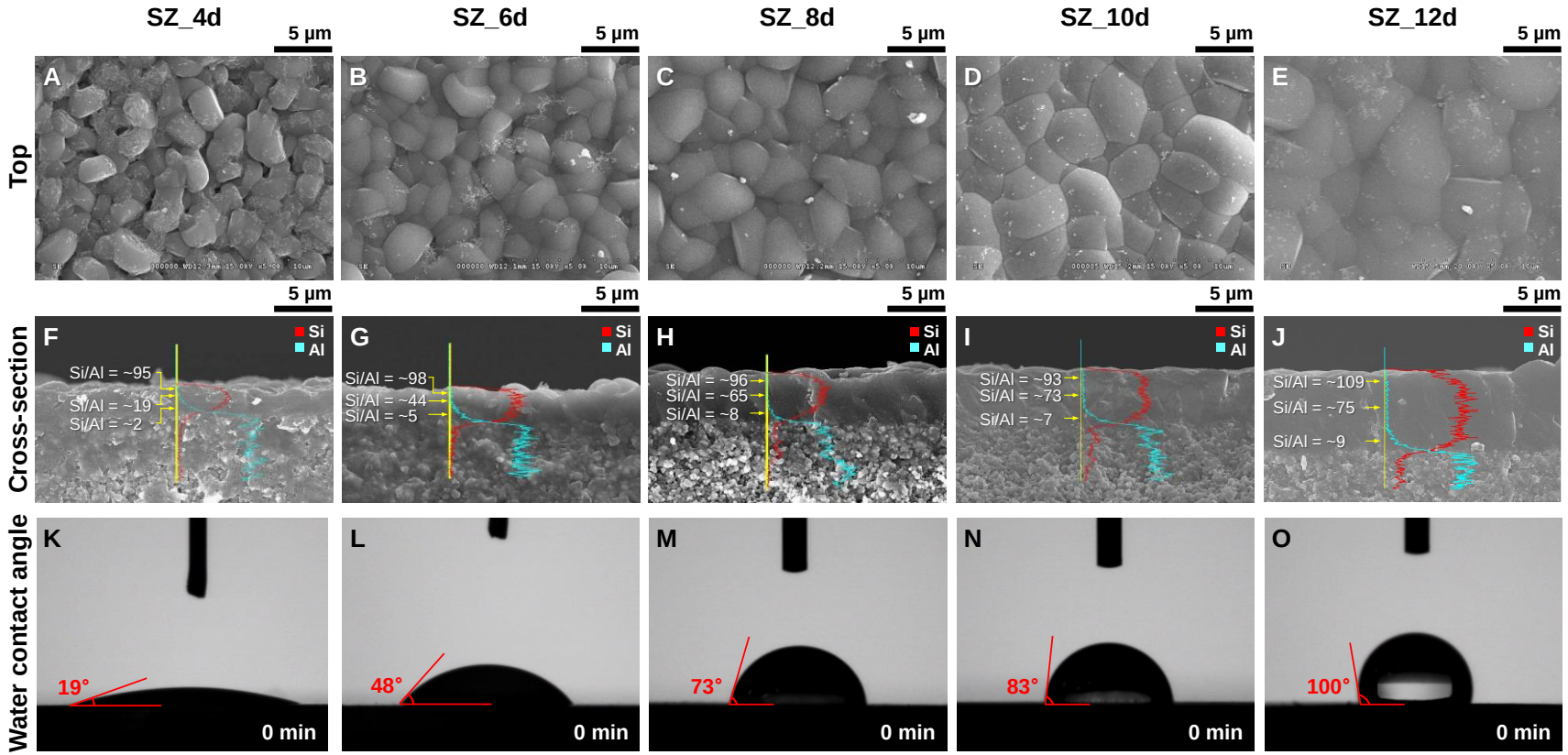

Fig. S7. Surface morphology, chemical composition, and hydrophobicity of the SZ membrane series. SEM images in (**A** to **E**) top view and (**F** to **J**) cross-sectional view of SZ_*x*d (*x* = 4, 6, 8, 10, and 12) along with (**K** to **O**) the images of the contact angle of a water droplet immediately after dropping a water droplet onto the surface. In (F to J), the EDX results with respect to the Si (red) and Al (cyan) atoms were obtained and are displayed along the yellow lines.

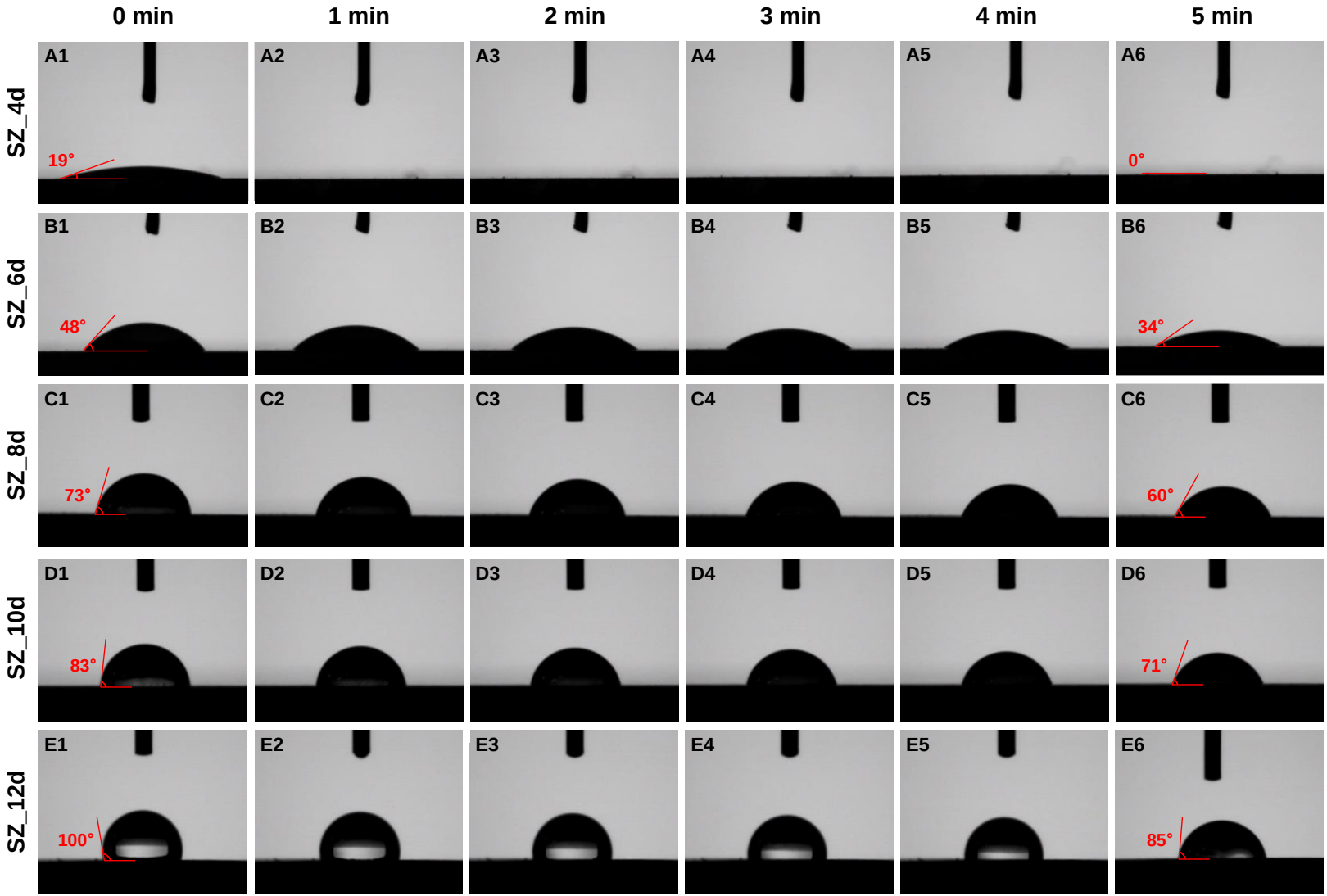

Fig. S8. Hydrophobicity of the SZ membrane series. Contact angle of a water droplet on SZ_*x*d; (**A1**)-(**A6**) *x* = 4, (**B1**)-(**B6**) *x* = 6, (**C1**)-(**C6**) *x* = 8, (**D1**)-(**D6**) *x* = 10, and (**E1**)-(**E6**) *x* = 12, as a function of time for up to 5 min.

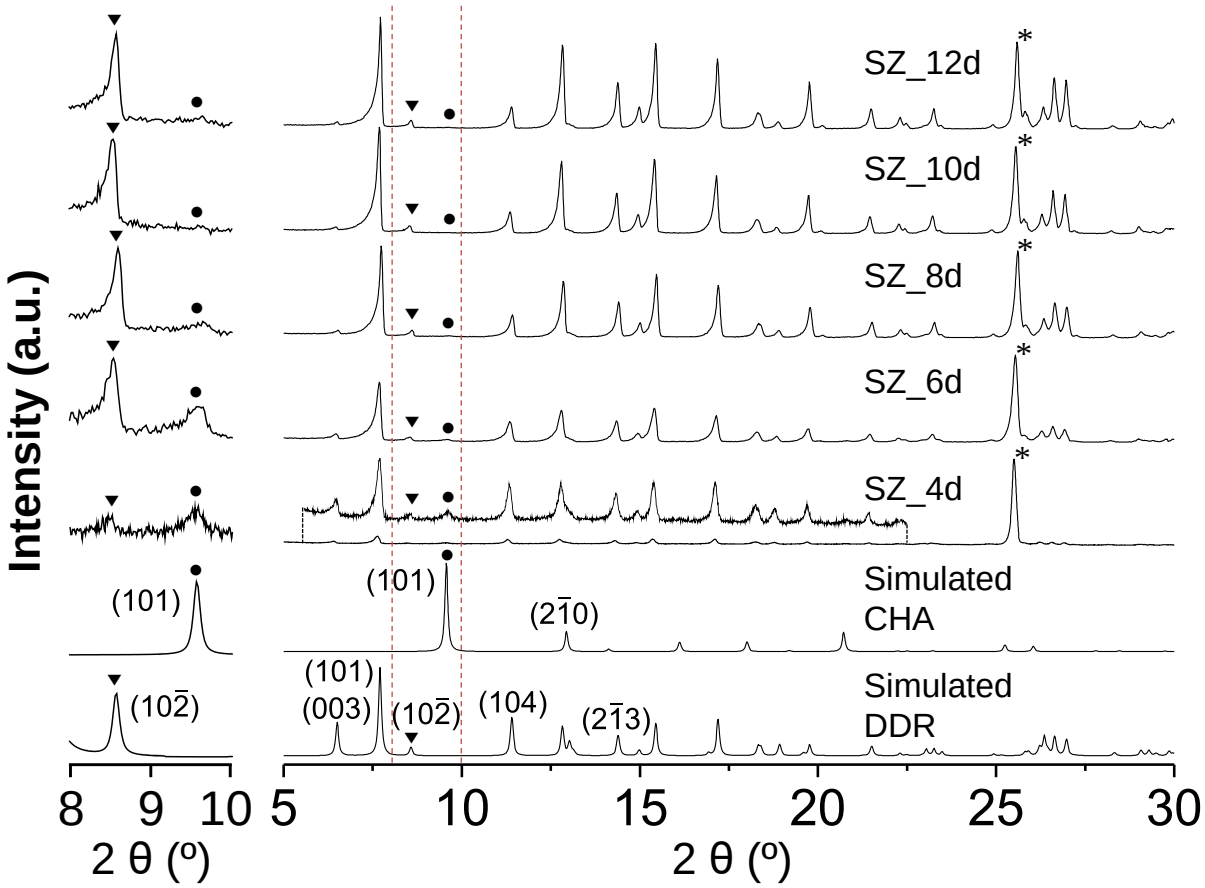

Fig. S9. XRD results of the hetero-epitaxially grown SZ membrane series. XRD patterns of SZ_*x*d (*x* = 4, 6, 8, 10, and 12). For better comparison, magnified XRD patterns in the 2 θ range from 8° to 10° are shown in the left. The inverted triangles (▼) indicate XRD peaks corresponding to the $(1\bar{0}2)$ plane of the DDR zeolite, and the circles (●) indicate XRD peaks corresponding to the (101) plane of the CHA zeolite. In addition, the simulated XRD patterns of all-silica DDR and CHA zeolites are shown at the bottom of the graph. Finally, the asterisks (*) denote the XRD peaks from the α-Al_2O_3 disc.

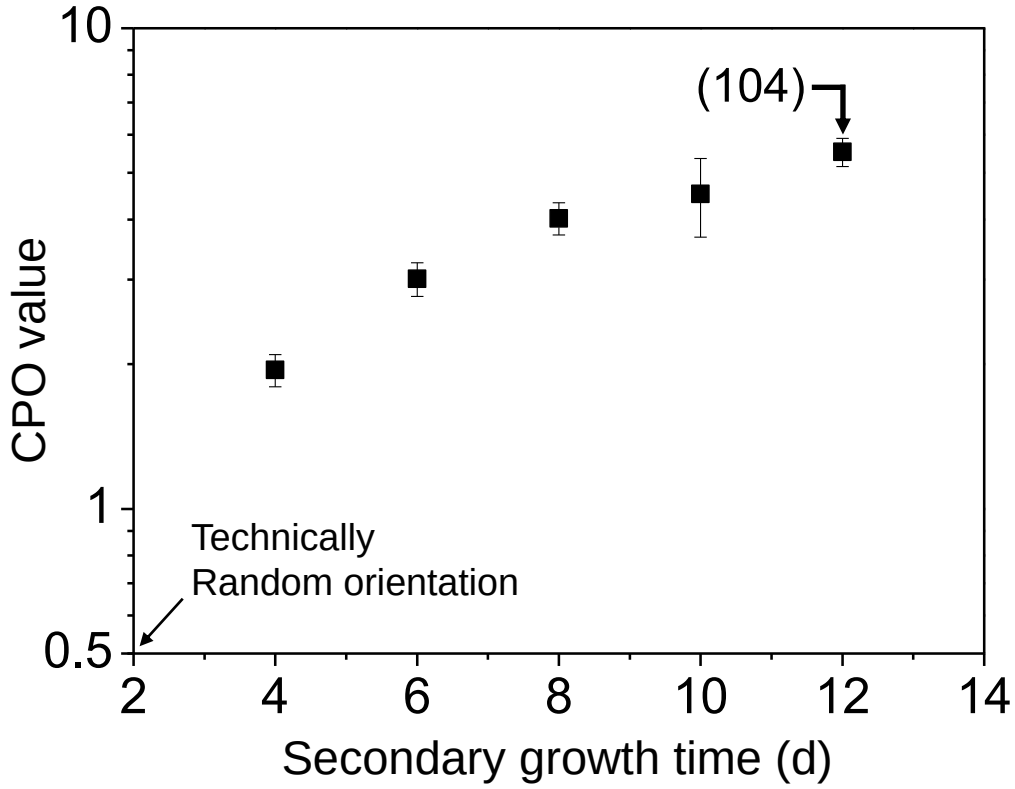

Fig. S10. CPO values of the SZ membrane series as a function of secondary growth time. For the CPO value, the ratios of the XRD peak areas of the (101) plane to those of the (104) plane were calculated.

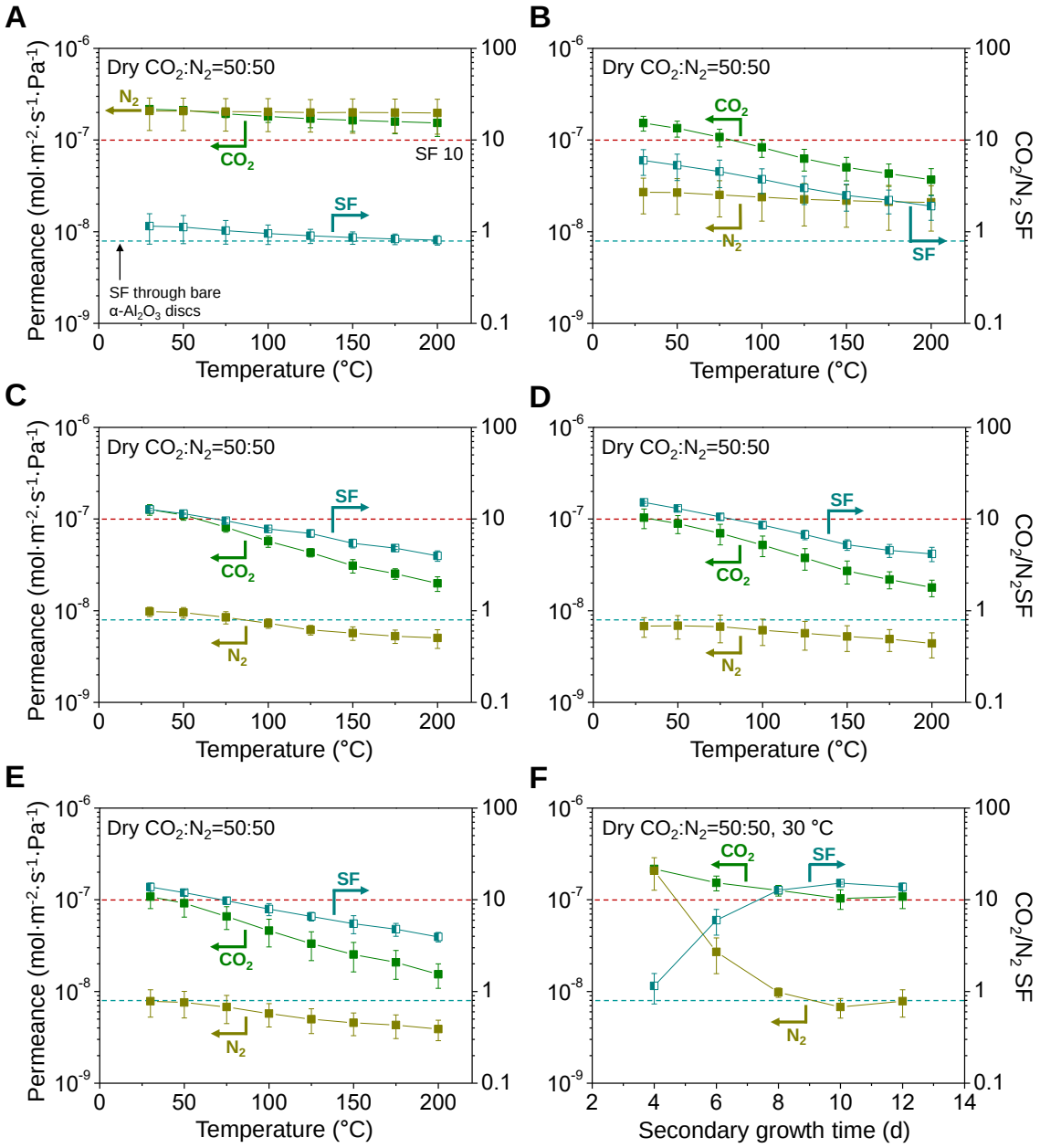

Fig. S11. CO_2/N_2 separation performances according to secondary growth time. (**A** to **E**) CO_2 and N_2 permeances and the corresponding CO_2/N_2 SFs through SZ_*x*d (*x* = 4 (A), 6 (B), 8 (C), 10 (D), and 12 (E)) with respect to equimolar CO_2/N_2 binary feed mixtures. The separation performances are plotted as a function of temperature up to 200 °C. In addition, CO_2/N_2 separation performances of SZ_*x*d (*x* = 4, 6, 8, 10, and 12) at 30 °C are collected in (**F**) and displayed as a function of secondary growth time (*x* in d). For comparison, the red dashed line indicates a CO_2/N_2 SF of 10 (as a result of the product of the diffusional and sorption selectivities) (*66*) and the cyan dashed line indicates a CO_2/N_2 SF of 0.8 (observed under Knudsen diffusion) through a bare α-Al_2O_3 disc, respectively.

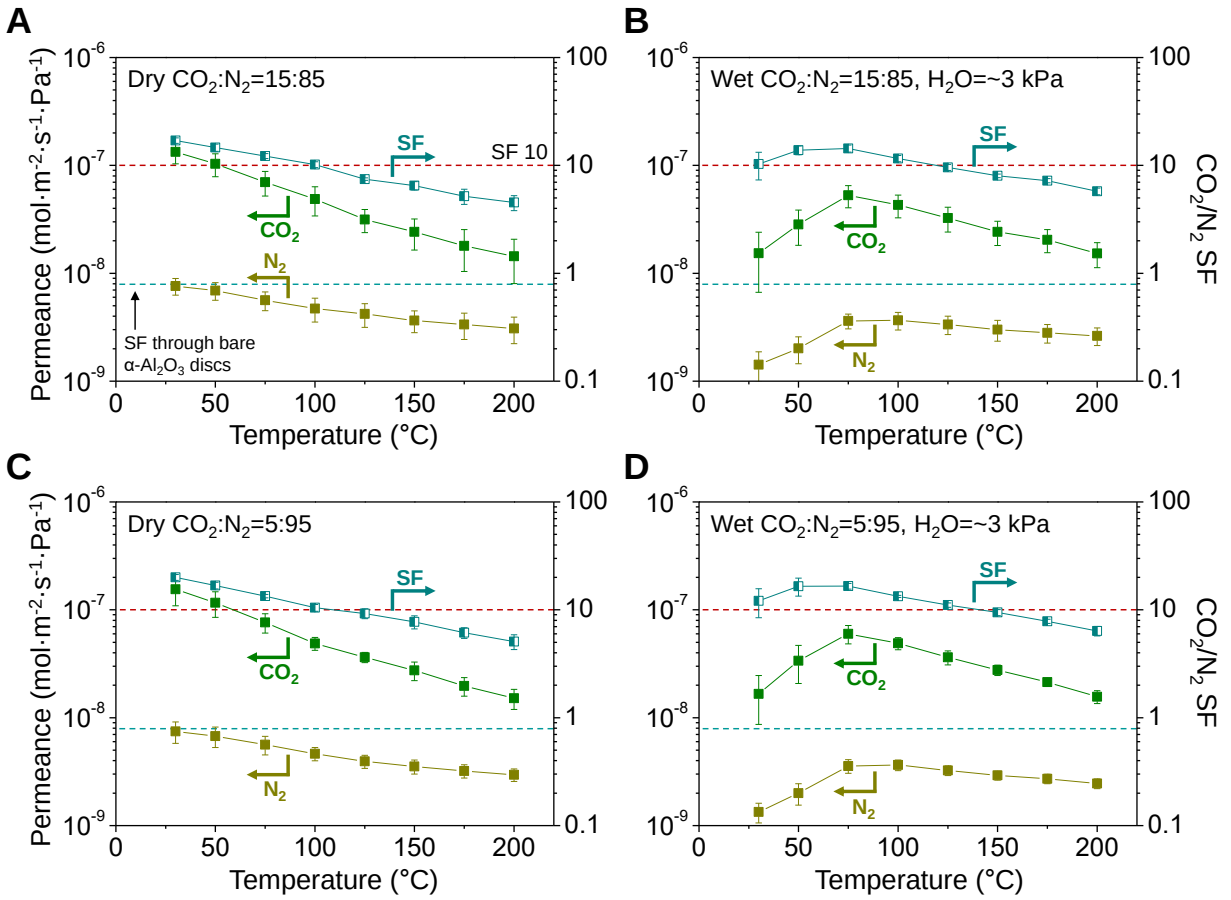

Fig. S12. CO_2/N_2 separation performances according to the molar composition of CO_2/N_2 in the feed. (**A** to **D**) Permeances of CO_2 and N_2 and corresponding CO_2/N_2 SFs through SZ_10d with CO_2/N_2 binary feed mixtures composed of (A and B) 15% CO_2 and 85% N_2 (C and D) 5% CO_2 and 95% N_2 under (A and C) dry and (B and D) wet conditions as a function of temperature up to 200 °C. The red and cyan dashed lines indicate the CO_2/N_2 SFs of 10 and 0.8, respectively.

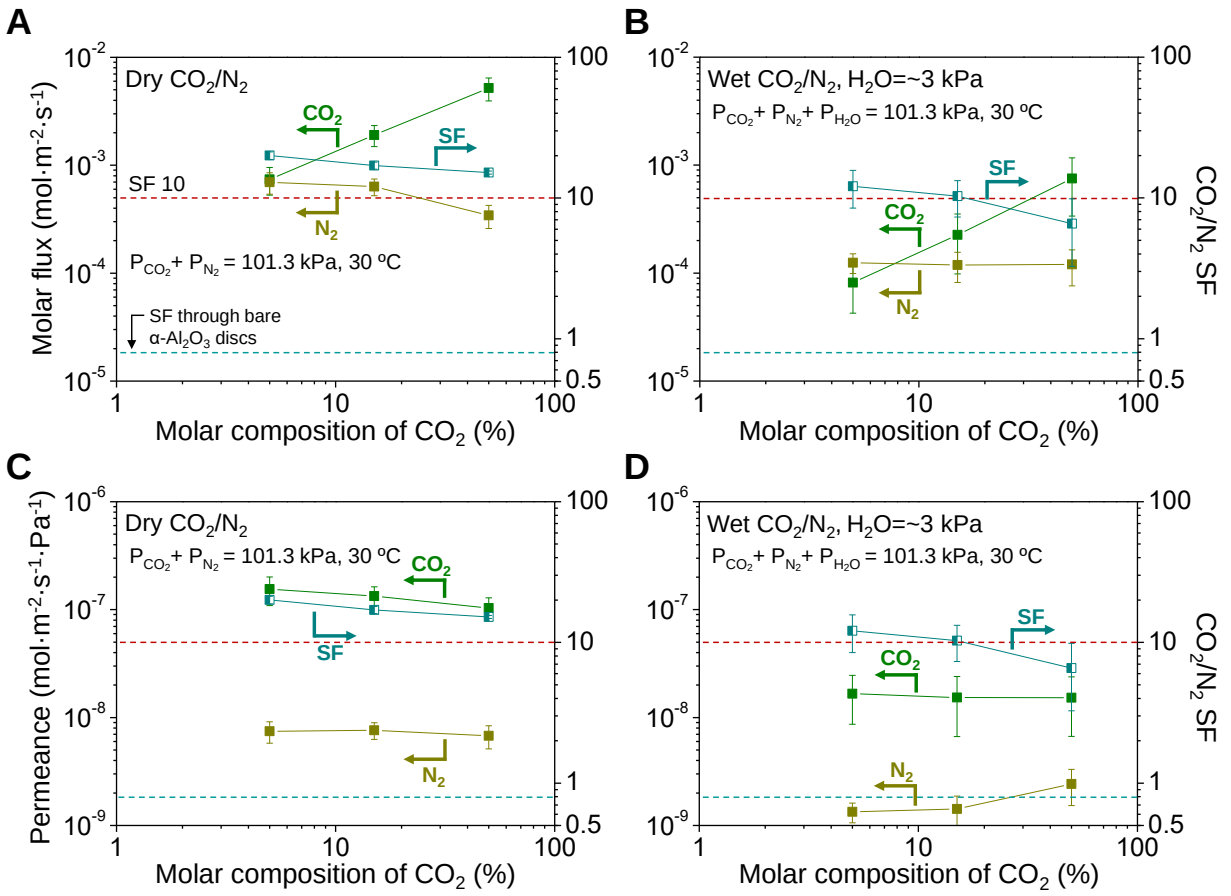

Fig. S13. Effect of the molar composition of CO_2/N_2 in the feed on the CO_2/N_2 separation performance. CO_2/N_2 (**A** and **B**) molar fluxes and (**C** and **D**) permeances and corresponding CO_2/N_2 SFs of SZ_10d with respect to the molar composition of CO_2 (5%, 15%, and 50%) at 30°C under dry and wet conditions. The red and cyan dashed lines indicate CO_2/N_2 SFs of 10 and 0.8, respectively.

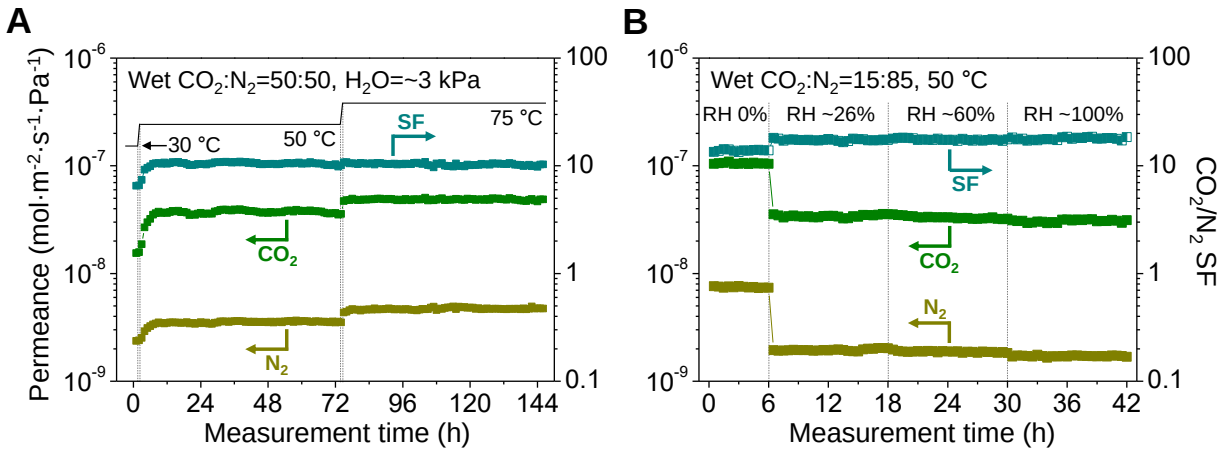

Fig. S14. Long-term stability test of SZ_10d under wet conditions. Stability tests of SZ_10d tested by changing the (**A**) temperature and (**B**) relative humidity of the measurement conditions. For (A), the temperature was maintained at 50 and 75 °C for 3 d, respectively, in equimolar CO_2/N_2 binary feed mixtures with H_2O vapor (3 kPa). For (B), the relative humidity was changed from 0% through ~26% and ~60% to ~100% (corresponding to water partial pressures of 0, ~3, ~7, and ~12 kPa, respectively) at 50 °C in CO_2/N_2 binary feed mixtures composed of 15% CO_2 and 85% N_2.

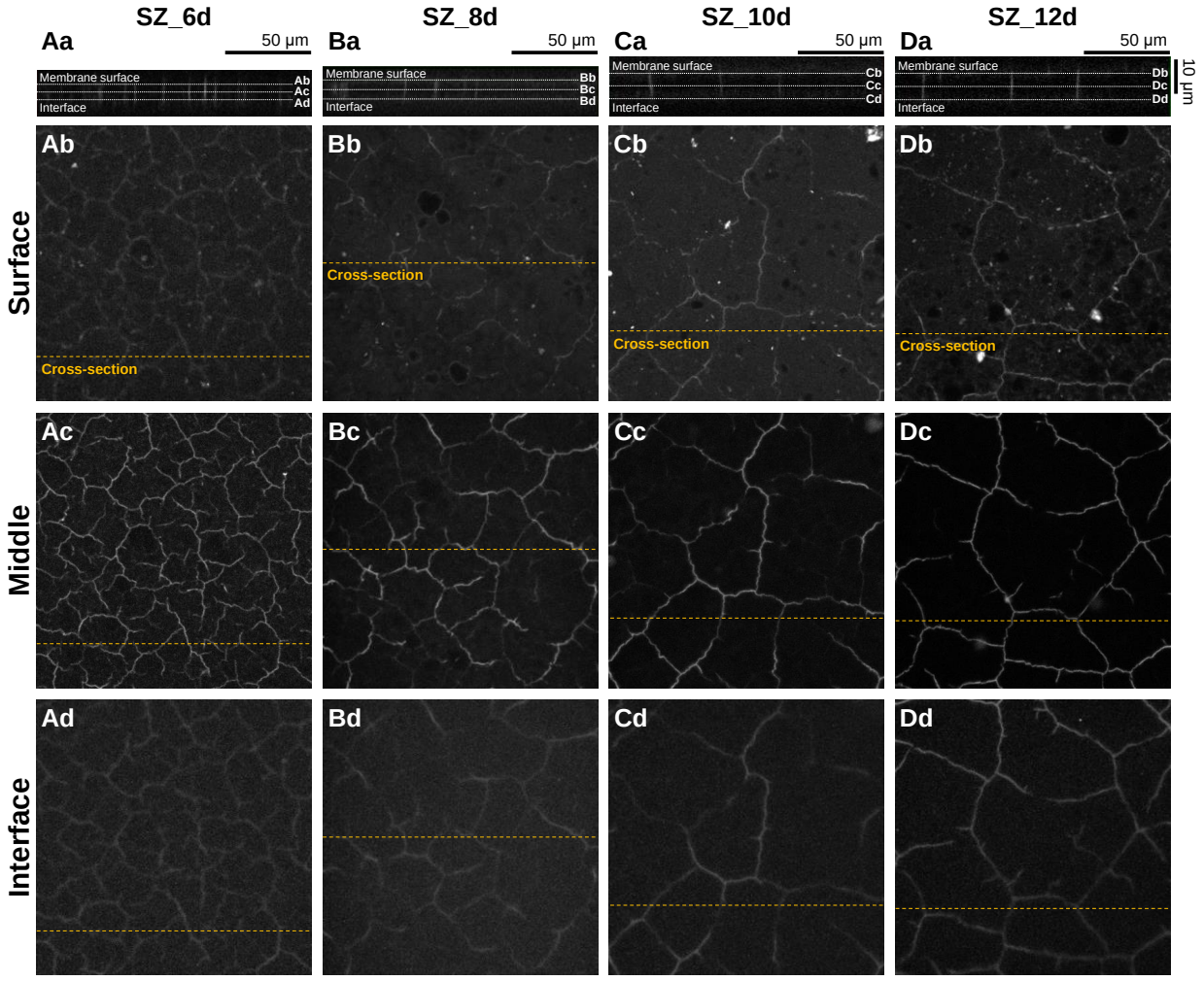

Fig. S15. FCOM characterization of the SZ membrane series. FCOM images of SZ_*x*d; (**Aa** to **Ad**) *x* = 6, (**Ba** to **Bd**) *x* = 8, (**Ca** to **Cd**) *x* = 10, and (**Da** to **Dd**) *x* = 12. The 1st row shows the cross-sectional view FCOM images and the 2nd to 4th rows show top view FCOM images obtained (Ab to Db) at the membrane surface, (Ac to Dc) in the middle area, and (Ad to Dd) at the interface between the membrane and α-Al_2O_3 disc. The cross-sectional view FCOM images were obtained at orange dashed lines of the top view FCOM images. White dashed lines in the cross-sectional view FCOM images indicate each position of the top view FCOM images shown in (yb)-(yd), where y = A, B, C, and D. (Ac)-(Dc) The top view FCOM images of the middle area were obtained at approximately 2, 3, 3.5, and 3.75 μm below the membrane surface, respectively.

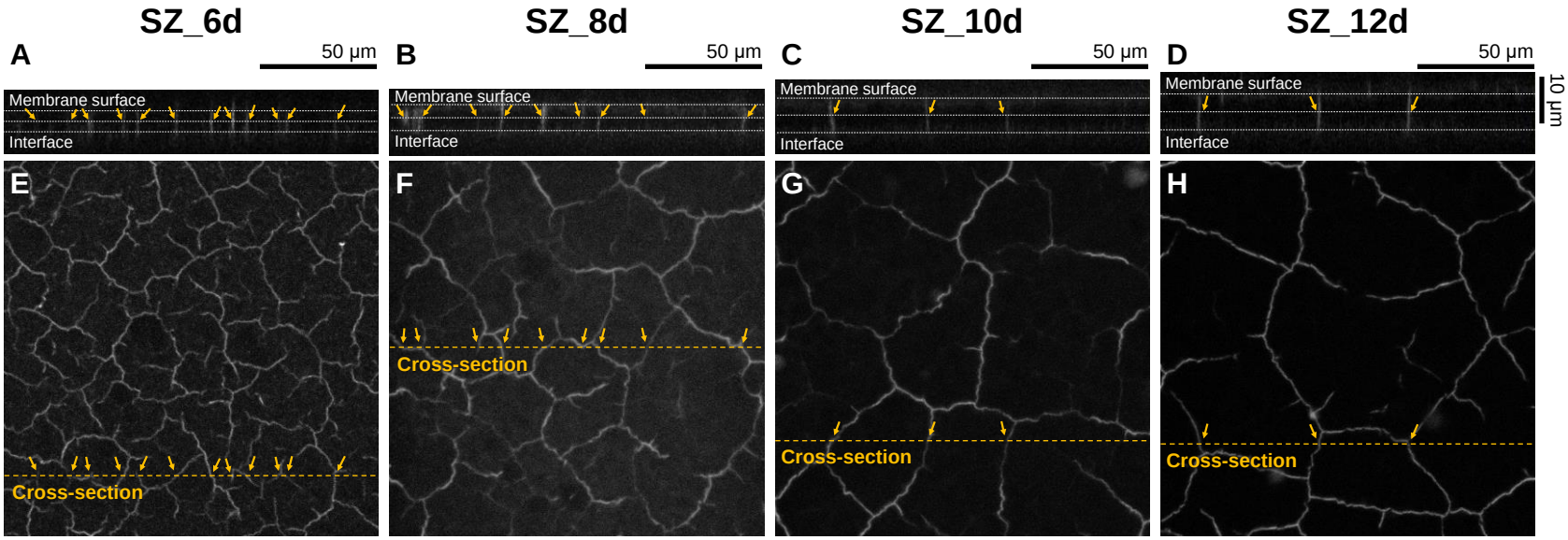

Fig. S16. FCOM characterization of the SZ membrane series. (**A** to **D**) Cross-sectional view and (**E** to **H**) top view FCOM images of SZ_*x*d (*x* = 6, 8, 10, and 12). In (A to D), the upper, central, and lower white dashed lines designate the membrane surface, the middle area and the interface between the membrane and the α-Al_2O_3 disc, respectively. The top view FCOM images in (E to H) were obtained at approximately 2, 3, 3.5, and 3.75 μm below the membrane surface, respectively (i.e., the 2nd row white dashed line in the cross-sectional FCOM images). The cross-sectional view FCOM images were obtained at orange dashed lines. For clarification, orange arrows are included to point to defects present in each membrane.

References and Notes

47. H. Kalipcilar, T. C. Bowen, R. D. Noble, J. L. Falconer, Synthesis and separation performance of SSZ-13 zeolite membranes on tubular supports. *Chem. Mater.* **14**, 3458-3464 (2002).
48. H. Robson, How to read a patent. *Microporous Mesoporous Mater.* **22**, 551-551 (1998).
49. J. Kuhn, J. Gascon, J. Gross, F. Kapteijn, Detemplation of DDR type zeolites by ozonication. *Microporous Mesoporous Mater.* **120**, 12-18 (2009).
50. E. Kim *et al.*, An Oriented, siliceous Deca-dodecasil 3R (DDR) zeolite film for effective carbon capture: insight into its hydrophobic effect. *J. Mater. Chem. A* **5**, 11246-11254 (2017).
51. E. Kim, W. Cai, H. Baik, J. Choi, Uniform Si-CHA zeolite layers formed by a selective sonication-assisted deposition method. *Angew. Chem. Int. Edit.* **52**, 5280-5284 (2013).
52. T. C. Merkel, H. Q. Lin, X. T. Wei, R. Baker, Power plant post-combustion carbon dioxide capture: an opportunity for membranes. *J. Membr. Sci.* **359**, 126-139 (2010).
53. D. Singh, E. Croiset, P. L. Douglas, M. A. Douglas, Techno-economic study of CO_2 capture from an existing coal-fired power plant: MEA scrubbing vs. O_2/CO_2 recycle combustion. *Energy Convers. Manag.* **44**, 3073-3091 (2003).
54. D. M. D'Alessandro, B. Smit, J. R. Long, Carbon dioxide capture: prospects for new materials. *Angew. Chem. Int. Edit.* **49**, 6058-6082 (2010).
55. M. Mofarahi, Y. Khojasteh, H. Khaledi, A. Farahnak, Design of CO_2 absorption plant for recovery of CO_2 from flue gases of gas turbine. *Energy* **33**, 1311-1319 (2008).
56. X. C. Xu, C. S. Song, B. G. Miller, A. W. Scaroni, Adsorption separation of carbon dioxide from flue gas of natural gas-fired boiler by a novel nanoporous "molecular basket" adsorbent. *Fuel Process. Technol.* **86**, 1457-1472 (2005).
57. M. Halmann, A. Steinfeld, Fuel saving, carbon dioxide emission avoidance, and syngas production by tri-reforming of flue gases from coal- and gas-fired power stations, and by the carbothermic reduction of iron oxide. *Energy* **31**, 3171-3185 (2006).
58. O. Bolland, S. Saether, New concepts for natural-gas fired power-plants which simplify the recovery of carbon-dioxide. *Energy Convers. Manag.* **33**, 467-475 (1992).
59. G. Bonilla, M. Tsapatsis, D. G. Vlachos, G. Xomeritakis, Fluorescence confocal optical microscopy imaging of the grain boundary structure of zeolite MFI membranes made by secondary (seeded) growth. *J. Membr. Sci.* **182**, 103-109 (2001).
60. J. Choi *et al.*, Grain boundary defect elimination in a zeolite membrane by rapid thermal processing. *Science* **325**, 590-593 (2009).
61. T. Lee, J. Choi, M. Tsapatsis, On the performance of c-oriented MFI zeolite membranes treated by rapid thermal processing. *J. Membr. Sci.* **436**, 79-89 (2013).
62. E. Kim, W. X. Cai, H. Baik, J. Nam, J. Choi, Synthesis and sonication-induced assembly of Si-DDR particles for close-packed oriented layers. *Chem. Commun.* **49**, 7418-7420 (2013).
63. J. Choi, S. Ghosh, Z. P. Lai, M. Tsapatsis, Uniformly a-oriented MFI zeolite films by secondary growth. *Angew. Chem. Int. Edit.* **45**, 1154-1158 (2006).
64. J. F. Yu, C. C. Qi, J. X. Zhang, C. Bao, H. Y. Xu, Synthesis of a zeolite membrane as a protective layer on a metallic Pd composite membrane for hydrogen purification. *J. Mater. Chem. A* **3**, 5000-5006 (2015).

65. J. F. Yu *et al.*, Controllable growth of defect-free zeolite protective layer on the surface of Pd membrane for chemical stability enhancement. *Microporous Mesoporous Mater.* **244**, 119-126 (2017).
66. E. Kim *et al.*, Mono-dispersed DDR zeolite particles by seeded growth and their CO_2, N_2, and H_2O adsorption properties. *Chem. Eng. J.* **306**, 876-888 (2016).
67. S. Himeno *et al.*, Synthesis and permeation properties of a DDR-type zeolite membrane for separation of CO_2/CH_4 gaseous mixtures. *Ind. Eng. Chem. Res.* **46**, 6989-6997 (2007).
68. A. Gouzinis, M. Tsapatsis, On the preferred orientation and microstructural manipulation of molecular sieve films prepared by secondary growth. *Chem. Mater.* **10**, 2497-2504 (1998).